ISPRS Journal of Photogrammetry and Remote Sensing 225 (2025) 196–220

Contents lists available at ScienceDirect

ISPRS Journal of Photogrammetry and Remote Sensing

journal homepage: www.elsevier.com/locate/isprsjprs

PRISMA imaging for land covers and surface materials composition in urban and rural areas adopting multiple endmember spectral mixture analysis (MESMA)

Giandomenico De Luca [a,*], Jose Luis Pancorbo [a], Federico Carotenuto [b], Beniamino Gioli [a], Giuseppe Modica [c], Lorenzo Genesio [a]

[a] Institute of BioEconomy (IBE), National Research Council of Italy (CNR), Via Madonna del Piano 10, 50145 Sesto Fiorentino, Italy
[b] Institute of BioEconomy (IBE), National Research Council of Italy (CNR), Via Piero Gobetti 11, 40129 Bologna, Italy
[c] Department of Veterinary Sciences, University of Messina, Viale G. Palatucci 12, I-98168 Messina, Italy

ARTICLE INFO

Keywords:
spectral mixture analysis (SMA)
Endmemebers selection
Land cover classification
Satellite hyperspectral
Remote sensing
Urban planning
Airborne hyperspectral
Spatial resolution

ABSTRACT

Covers and surface materials composition of urban, *peri*-urban and rural landscapes is significant information for environmental, climate and human-ecosystems interaction monitoring and modeling, as well as for addressing specific urban planning and improving environmental management. In this study the multiple endmember spectral mixture analysis (MESMA) was exploited to overcome the low spatial resolution and spectral mixture of the hyperspectral (HS) satellite PRISMA (*PRecursore IperSpettrale della Missione Applicativa*). A multi-level detail large-scale mapping of complex urban and rural fractional composition of land covers and surface materials (LCSM) was carried out. High-resolution airborne data enabled the collection of pure endmembers for each impervious and pervious surface materials, also acting as a reference for assessing resulted sub-pixel fractional covers at the pixel scale. Absolute Errors (AE) have shown that MESMA is very promising for quantifying complex landscape composition at the sub-pixel level from PRISMA HS data (overall AE <=0.282; per-class AE < 0.336, with average values even < 0.1 for some classes). Bias Errors (BE) instead attested that under- and overestimation errors for each class were contained in ±0.25 median values for all three levels of detail (i.e., number of classes) tested. These results demonstrate that the proposed framework integrating MESMA and PRISMA HS is a valuable tool to provide detailed land composition in complex landscapes to support urban planning and enhance environmental sustainability.

1. Introduction

The complexity and heterogeneity of urban and rural landscapes poses challenges for the characterization and mapping of their various physical and biophysical components (García-Pardo et al., 2023; McPhearson et al., 2016; Weng, 2012). As a result of anthropogenic development, the expansion of impervious surfaces – i.e. artificial surfaces covered by water-resistant materials (e.g. asphalt, concrete, etc.) – brings well-known impacts on the biotic and abiotic properties of surrounding ecosystems, even those distant from urban areas (Grimm et al., 2008). At the same time, the mitigation effects and services provided by these ecosystems and/or agro-ecosystems located in *peri*-urban areas must also be equally considered (McDonald et al., 2013; Müller et al., 2013; Mulya et al., 2023). Updated and detailed spatialized information on urban and rural landscape composition, as well as pervious-impervious surfaces ratio quantification, are therefore fundamental to assess the pressures of anthropic development on the environment (Cavalli, 2022; Grimm et al., 2008; Vavassori et al., 2023), the hydrological impacts of soil sealing (Wang et al., 2022), and the effects of air pollution on land and water habitats (Chen et al., 2022). It is also crucial for monitoring the ecological interconnections between urbanized surface and surrounding ecosystems (Lumia et al., 2023) and/or agro-ecosystems (Mulya et al., 2023), as well as for tracking land consumption (Luti et al., 2021) and quantifying existing vegetation inside urban and *peri*-urban context (García-Pardo et al., 2023). This understanding is essential for accurately scaling climate-related models – e.g. emission estimation (Huang et al., 2022), carbon stock change assessment (Brilli et al., 2022; Brilli et al., 2019), surface albedo retrieval (Wu et al., 2022),

* Corresponding author.
E-mail address: giandomenico.deluca@cnr.it (G. De Luca).

https://doi.org/10.1016/j.isprsjprs.2025.04.038
Received 7 November 2024; Received in revised form 4 April 2025; Accepted 28 April 2025
Available online 4 May 2025
0924-2716/© 2025 The Author(s). Published by Elsevier B.V. on behalf of International Society for Photogrammetry and Remote Sensing, Inc. (ISPRS). This is an open access article under the CC BY license (http://creativecommons.org/licenses/by/4.0/).

meteorological modelling (Yu and Leng, 2022) – and for guiding the implementation of specific emission reduction actions and achieving climate neutrality in line with goals set by local, national, and international institutions (e.g. European Green Deal). In general, to support sustainable urban, *peri*-urban and rural planning and management (McPhearson et al., 2016; Vavassori et al., 2023; Weng, 2012; Xu et al., 2019).

In addressing this complexity, remote sensing offers substantial information in terms of spatial and temporal scales (Cavalli, 2021; Franke et al., 2009; García-Pardo et al., 2023; Weng, 2012), providing a more efficient alternative to costly and time-consuming field-based measurements (García-Pardo et al., 2023, 2022; Neyns and Canters, 2022). Remote sensing approaches based on multispectral (MS) and high-resolution airborne hyperspectral (HS) data have long been used for mapping land cover composition, allowing detailed distinction of surface materials (such as infrastructures, building cover materials, vegetation, soils, etc.) (Feng and Wang, 2018; van der Linden et al., 2019; Vavassori et al., 2023; Weng, 2012). The use of optical sensors to identify spatial patterns of impervious surfaces and natural elements including both photosynthetic and non-photosynthetic vegetation (NPV) within urban and *peri*-urban areas has become a recognized method to assess ecosystem services, or to instruct the development of further investigation protocols (Behling et al., 2015; García-Pardo et al., 2022; van der Linden et al., 2019). While MS data are widely available, they provide limited information on the spectral complexity of urban and *peri*-urban areas. On the other hand, the high economic costs associated with airborne HS data constrain their acquisition's temporal frequency and spatial coverage (Weng, 2012; Xu et al., 2019). The rise of HS satellites, however, is introducing new opportunities and challenges for large-scale medium-resolution mapping, allowing for the use of detailed spectral information that is crucial for analyzing complex landscapes.

Among the most recent HS space missions, PRISMA (*PRecursore IperSpettrale della Missione Applicativa*) is the Italian Space Agency's (ASI) HS spectrometer which relies on an innovative prism-based optical instrument (Loizzo et al., 2019). Launched in March 2019 with the primary goal of assessing the capability to monitor Earth's land surfaces and atmosphere as a precursor to future missions, PRISMA is nearing the conclusion of an initial independent scientific calibration and validation phase. This phase, conducted as part of the PRISCAV project (PRISMA CAL/VAL), covers a set of selected study areas with various land cover types and uses (Cogliati et al., 2021; De Luca et al., 2024; Guarini et al., 2018; Loizzo et al., 2019; Pepe et al., 2023, 2020; Pignatti et al., 2022; Pignatti et al., 2013).

Despite the potential of HS spaceborne imagery, relatively few studies have included these data (e.g., Cavalli, 2023; Cavalli et al., 2008; Demarchi et al., 2012; Fan & Deng, 2014; Weng et al., 2008), or at least simulated systems (Clark, 2016; Clasen et al., 2015; Dennison et al., 2019; Feng and Wang, 2018), in the framework of detailed mapping of urban and rural surfaces composition. While HS satellite data potentially offer higher temporal resolution and broad coverage, enhancing spatio-temporal scene analysis, their primary shortcoming lies in pixel resolution. This limitation arises from the trade-off between signal-to-noise ratio (SNR) and ground sample distance (GSD) (Yokoya et al., 2017), leading to a lack of the spatial detail necessary for many urban, *peri*-urban and rural analysis and mapping applications (van der Linden et al., 2019). Urban and *peri*-urban landscapes, shaped by intensive human activities, are highly fragmented in a wide range of biophysical and biochemical attributes, leading to high intra-class spectral diversity and significant inter-class spectral similarity. As GSD increases, these factors make pixel-level classification unrealistic, raising the prevalence of mixed pixels as a major challenge in mapping such environments using medium spatial resolution images (Cao et al., 2022; Degerickx et al., 2019; Franke et al., 2009; Small, 2005, 2003; Xu et al., 2019). Spectral mixture analysis (SMA) is considered the ideal approach to address mixed spectral information in such complex conditions (Small, 2005, 2003). SMA has been widely applied to deal with the mixed pixel problem (Cavalli, 2023, 2022, 2021; Fan and Deng, 2014; Franke et al., 2009; Weng, 2012; Wu et al., 2014; Xu et al., 2019). SMA operates on the assumption that each image pixel's spectrum is a mixture of spectral signals (mixed pixels), each representing a specific component, object, or surface present within that portion of Earth's surface (Adams et al., 1993). Unlike classification algorithms, SMA provides a measure of the fractional abundance of specific materials at the sub-pixel level, offering a physical description of the observed surface (De Luca et al., 2023; Franke et al., 2009; van der Linden et al., 2019). However, traditional SMA models, which apply a fixed single set of endmembers across an entire scene (e.g., Linear SMA (Shimabukuro and Ponzoni, 2019), work reasonably well in areas with relatively homogeneous land covers but are less effective in complex urban and *peri*-urban contexts due to their limited ability to account for within-class variability (Deng and Wu, 2016; Wu et al., 2014). Since its proposal by Roberts et al. (1998), Multiple Endmember Spectral Mixture Analysis (MESMA) has emerged as the most popular alternative to traditional unmixing techniques (Degerickx et al., 2019; Fan and Deng, 2014) finding application in various environmental studies since its introduction (Demarchi et al., 2012; Fernandez-Manso et al., 2016; Pancorbo et al., 2023; Quintano et al., 2020, 2017). MESMA, commonly defined as an optimized extension of SMA, allows different endmembers of the same surface material to be tested and selected to characterize each individual pixel, thereby better accounting for endmember variability and more accurately modeling spectral heterogeneity across the scene (Fan and Deng, 2014; Franke et al., 2009; Roberts et al., 1998; Veraverbeke et al., 2012).

As with any SMA approach, MESMA's effectiveness relies on the accuracy of the endmembers' representativeness (Dennison and Roberts, 2003; Fan and Deng, 2014; Somers et al., 2011). Generally, a sample of pure endmembers extracted from the same observed image have proved to be optimal due to the consistency of brightness details with those of the scene (De Luca et al., 2023; Demarchi et al., 2012), and the alignment with the vegetation's physiological stage (Meerdink et al., 2019). However, medium/coarse GSDs and complex landscape textures often compromise the distinct spectral signatures of impervious surface materials, making it challenging to find individual pixels pure enough to uniquely define them. To address these challenges, high spatial resolution HS imaging data – i.e. from airborne or unmanned aerial vehicle (UAV) – simultaneously acquired to satellite data (coherent lighting conditions), provide an alternative method to construct or complement reference spectral libraries (van der Linden et al., 2019).

Among the very few applications of MESMA on HS satellite data, only four have applied this algorithm to PRISMA data: two for fire severity (Quintano et al., 2023) and fire risk (Fernández-Manso et al., 2024) characterization; another for mapping invasive palm species (Damarjati et al., 2022); the study of Cavalli (2023) applied MESMA to PRISMA data in an urban context to evaluate the impact of different sensor features in retrieving urban characteristics.

Therefore, in light of this limited prior research, the present study represents a groundbreaking effort to utilize MESMA to retrieve and map urban, *peri*-urban and rural composition from PRISMA HS satellite data. The approach was tested in two historical Italian cities, Prato and Lucca, as well as in two areas of historically significant rural landscapes, Grosseto and Arborea, both of which have been previously monitored within the PRISCAV project. Endmembers were extracted from high-resolution aerial HS imagery acquired simultaneously with the satellite data. Qualitative and spatial validation of SMA results is often lacking in the literature due to the absence of detailed independent reference data (Cavalli, 2022). To address this gap, the present study utilized the airborne HS images to generate a high-resolution land cover and surface materials (LCSM) classification map using a random forest (RF) machine learning algorithm. This approach allowed for a comparative analysis to assess the consistency of the results.

The primary objectives of this study were therefore to: (i) apply MESMA on PRISMA HS imagery for the retrieval and mapping of LCSM

fractional abundance for the first time; (ii) overcome the challenges of obtaining pure reference endmembers by leveraging high-resolution simultaneous airborne spectrometry; and (iii) use such high-resolution dataset to validate and assess the consistency of the approach proposed.

2. Data and methods

2.1. Study areas

The study was conducted on two historic cities in central Italy, Prato (43°52′48″N, 11°05′54″E) and Lucca (43°50′37″N, 10°30′18″E), and on two areas of historically significant agriculture landscapes, the rural area in the north-west part of Grosseto city (42°52′13.5″N, 11°03′53″E), and the area around Arborea town (39°46′20.9″N 8°34′49.8″E). The study areas share similar characteristics, with diverse types of pervious land covers and complex compositions of impervious materials. The *peri*-urban belts of Prato and Lucca are predominantly covered by agricultural fields, including green and non-photosynthetic vegetation, as well as bare soils (Arcidiaco and Corongiu, 2025). Natural and semi-natural forested areas are primarily located on hills and near water bodies. The rural areas are interspersed with a varied mix of residential zones, differing in density and socioeconomic structure—from scattered, isolated family houses with surrounding greenery to condominium complexes—and industrial districts. Arborea lies on a reclaimed plain, transformed in the early 20th century, which has since become a highly productive agricultural landscape. Both Grosseto and Arborea areas are characterized by a strong land fragmentation, with a pronounced mosaic pattern reflecting the diversification of crops and intensive agronomic management. The building materials in these areas range from traditional terracotta red tiles (*coppo*), concrete, and bitumen (used in roads and roofs) to various metals. Gravel, glass and plastic are scarcely present. Prato, in particular, is a significant and historic industrial hub, known for its textile sector, which has shaped the landscape of this territory. In both Prato and Lucca cities, the *peri*-urban belt is arranged concentrically around the historic center characterized by a cluster of traditional red tile roofs.

2.2. Image data and pre-processing

2.2.1. PRISMA hyperspectral (HS)

The PRISMA HS satellite is constituted by a Sun-synchronous low-Earth orbit push-broom image scanning mode, covering an across-track 30 km swath in 1000 pixels, with a field of view (FOV) of 2.77°, a 30 m of GSD. It has an orbital cycle of around 29 days, with a revisit pass < 7 days (off-nadir) via specific on-demand request. The sensor captures a spectral range between 400 and 2500 nm, distributed over 239 bands with spectral sampling interval < 12 nm, separated into two main spectral cubes: visible-near infrared (VNIR; 400–1000 nm, 66 bands) and shortwave infrared (SWIR; 1000–2500 nm, 173 bands). A panchromatic (400–700 nm) image is also provided with a 5 m GSD.

The L2D product, involving bottom-of-atmosphere (BOA) reflectance (MODTRAN-based atmospheric correction processor v.02.05), *ortho*-projected and geocoded (WGS 84 / UTM zone 32 N), was used in this study. Five cloud-free images were obtained: one for Prato (27th June 2020); two contiguous images for Lucca (27th July 2023), subsequently mosaicked using the Quick Mosaic algorithm in ENVI 5.6 software (NV5 Geospatial, Broomfield, Colorado, USA); one for Grosseto (31st July 2020); one for Arborea (30th May 2022). The mosaicked image of Lucca was clipped to reduce the size of the scene, considering that the city was decentralized towards the East of the image. A band selection procedure was conducted following a protocol previously developed (De Luca et al., 2024). The selection process included: (i) any defective bands with more than 90 % zero-valued pixels, including bands flagged as zero in the metadata; (ii) water vapor absorption spectral regions (1350–1470 nm, 1800–1950 nm, 922–961 nm, 1100–1140 nm, and 2020 nm); and (iii) bands with high levels of noise (e.g., 406.9–423.8 nm; 2342.8–2477.1 nm). The final dataset comprised 163 bands.

2.2.2. Airborne hyperspectral (HS)

The four study areas were surveyed by means of four dedicated flights utilizing two different airborne HS systems: HySpex for Prato on June 22nd 2020 and CASI/SASI for Lucca (on July 15th 2023), Grosseto (July 31st 2020) and Arborea (May 29th 2022). The HySpex system (Norsk Elektro Optikk, Norway) carries two separate push-broom sensors: the VNIR-1800, ranging between 400 and 1000 nm over 186 bands with a spectral sampling interval of 3.3 nm, and the SWIR-384, spanning 960 to 2500 nm over 288 bands with a spectral sampling interval of 5.5 nm. The spectral distance between the PRISMA HS central wavelengths and the HySpex sensors was $\leq \pm 2$ nm. The VNIR and SWIR sensors captured images with GSD of 1 m and 3 m, respectively. Similarly, the CASI/SASI system (Itres Research Ltd., Canada) features two push-broom scanners: the CASI-1500, which covers 380 to 1050 nm over 96 bands with a spectral sampling interval of 7.2 nm, and the SASI-600, which spans 950 to 2450 nm with 100 bands and a spectral sampling interval of 15 nm. The spectral distance between the PRISMA HS and CASI/SASI sensors did not exceed 3 nm for CASI and 7 nm for SASI across the entire spectral range. The GSD for CASI was 1.5 m and for SASI was 3.75 m.

The airborne HS images from both sensors were radiometrically corrected, *ortho*-projected, and geocoded (WGS 84 / UTM zone 32 N). Atmospheric correction was performed using the MODTRAN-based atmospheric radiative transfer model implemented in ATCOR-4 v.7.4.1 software (ReSe Applications LLC, Langeggweg 243 3, CH-9500 Wil SG, Switzerland), validated with in-situ reflectance and radiance data collected by a FieldSpec 3 spectroradiometer (Malvern Panalytical Ltd, Malvern, UK) during the overflight. VNIR and SWIR datasets from both systems were subsequently stacked and harmonized to a 3 m spatial resolution using nearest neighbor interpolation in ENVI v. 5.6 software. The datasets were then spectrally resampled to match the PRISMA spectral response function (SRF), reconstructed as a Gaussian function using the full width at half maximum (FWHM) with the Spectral Resampling tool in ENVI 5.6, after filtering out the same noisy wavelengths excluded for PRISMA (Section 2.2.1). The images were rescaled to floating-point format at 32 bits [0, 1], comparable to PRISMA. Finally, the airborne and PRISMA HS datasets were co-registered using the workflow proposed by the same research group (De Luca et al., 2024), which relies on the AROSICS open-source software (Scheffler et al., 2017).

A high-resolution, highly accurate classified map was also generated from the airborne hyperspectral dataset to compare with the MESMA outputs for assessment (Sesction 2.5). The random forest (RF) machine learning classification algorithm (Breiman, 2001) was employed, trained on a total of 5000 pixels for each study area, representing the ten LCSM classes (i.e. 500 points per surface type) defined in Section 2.3. The training pixels were carefully selected across the entire study area using the meticulous visual inspection criteria detailed in Section 2.3, with additional consideration given to capturing the full range of illumination conditions. This approach improved spectral variability representation and reduced misclassification due to shadow-induced lighting differences. Apart from the *number* and the *depth of trees*, RF hyperparameters were set with the default values provided by the Scikit-learn library (Pedregosa et al., 2011). The two former hyperparameters were set testing all possible combinations within a predefined set of values – *number of trees* {100, 500, 1000, 5000, 10000} and *tree depth* {10, 50, 100, 500, 1000} – and selecting the combination that achieved the best out-of-bag (OOB) score. All bands were included in the classification, with an additional edge texture feature calculated from the red band using the OrfeoToolBox EdgeExtraction application (OrfeoToolBox - OTB, 2024), adopting a gradient filter, and added to the dataset as extra spatial information to improve classification accuracy. An independent validation set of 1500 pixels per class was used to construct the confusion matrices for classification accuracy evaluation, achieving an overall

accuracy of over 90 % for all study areas. Fig. 1

2.3. Land cover classes definition and endmembers selection

A detailed visual analysis of high-resolution images – i.e. airborne HS true and false colors, spectral indices (the cellulose absorption index, CAI (Daughtry, 2001), supported the discrimination of NPV from bare soil), and RGB Google Imagery – combined with knowledge of the study areas, led to the identification of ten LCSM classes across both study areas (Fig. 2). The ten classes were selected as representative of the investigated urban landscape while being adequately distinguishable within the minimal GSD (airborne), as determined from preliminary investigations (Pancorbo et al., 2024). Furthermore, a literature review suggests that these classes might be adaptable to both nationally and internationally contexts (Cavalli, 2021; Kotthaus et al., 2014; Xu et al., 2019). For each class, pure spectral signatures (50 signatures per class and for each study area) were retrieved from the corresponding high-resolution airborne imagery, to develop a spectral library to feed the MESMA model described in Section 2.4 (Fig. 2, central column; a more detailed illustration of the endmembers is observable in Figs. S32-S41 of supplementary materials). Each signature was derived from a pure pixel that accurately represents each class. The reference pixels used to construct the spectral library were meticulously selected to ensure their purity (e.g., avoiding edge pixels) and were randomly and homogenously distributed across the entire scene to capture the full spectral variability.

Water bodies were excluded from the analyses due to their distinct spectral behavior (Braga et al., 2022; Giardino et al., 2020). They are, in fact, prone to specular reflections, which can introduce uncertainties when comparing spectra from multiple sensors, requiring ad-hoc analyses..

To address scene complexity, three hierarchical levels were defined and tested, grouping the spectral libraries into different levels of detail to create separate rearranged libraries for each level. Level-1 combined all classes into two broad categories: pervious and impervious. Level-2 grouped six classes based on LCSM color, while Level-3 provided the highest level of detail with all eleven individual classes. The hierarchy of these levels is illustrated in Table 1.

A preliminary statistical analysis was also conducted on the collected endmembers to retrieve intra- and inter-class spectral separability. The spectral angle mapping (SAM; eq. (1) was computed for the scope (Yuhas et al., 1992):

$$SAM = arccos(\langle x,y\rangle / ||x|| \cdot ||y||) \quad (1)$$

where x and y are two different endmembers. The SAM is expressed in radians, ranging between 0 (when endmembers are identical), and π (highest separability).

2.4. Multiple endmember spectral mixture analysis (MESMA)

MESMA was used to develop maps of subpixel LCSM fractional abundance (fractional images, FIs) by running and testing multiple combinations of the endmembers (Roberts et al., 1998). The algorithm evaluates the most suitable combination of endmembers for each pixel based on the number of recognized LCSMs. The optimal number of classes to unmix each pixel, as a linear combination of the respective endmembers, is determined using a threshold criterion based on root mean square error (RMSE) calculated from the residual errors of each model test (Demarchi et al., 2012; Dennison et al., 2019; Fan and Deng, 2014; Franke et al., 2009). The number of endmember models – i.e. the maximum number of components through which a pixel can be fractioned – is settable, ranging from 2 to the total number of classes used. In this study 2-, 3- and 4-endmmebers models were tested given their proven effectiveness in complex landscapes (Demarchi et al., 2012; Deng and Wu, 2016; Fan and Deng, 2014; Franke et al., 2009; Powell and Roberts, 2008; Quintano et al., 2023; Xu et al., 2019), natural environments (Dennison et al., 2019), and to avoid imbalances between estimated and actual components per pixel (Demarchi et al., 2012). Additionally, this range offers a reasonable balance between computational time and memory usage. The distribution of the unique number of airborne-derived LCSM classes within each PRISMA pixel was also analyzed to further support the selection of endmember models.

The MESMA algorithm iteratively compares models and selects the one with the lowest RMSE. If the relative reduction in RMSE between models with different complexities exceeds a predefined threshold, the algorithm opts for the model with more endmembers (Demarchi et al., 2012; Deng and Wu, 2016). A default RMSE threshold of 0.007 was adopted, as it is considered optimal according to the literature (Pancorbo et al., 2023; Roberts et al., 2012; Tane et al., 2018) and the software authors' recommendations (Roberts et al., 2019). To ensure physically realistic fractions, constraints for non-negative values and sum-to-one fractions were applied, while no maximum RMSE threshold or residual constraints were set to avoid unmodeled pixels in the output FIs. To account for brightness differences, an additional shade component with a default fraction of ≤ 0.8 was included and used to normalize MESMA outputs by dividing each fraction by the sum of non-shade fractions, as suggested in previous studies (Cao et al., 2022; Pancorbo et al., 2023; Quintano et al., 2020; Tane et al., 2018).

The spectral library described in Section 2.3 was subsequently filtered using the iterative endmember selection (IES) quality metric (Schaaf et al., 2011). This algorithm, known for its consistent accuracy in urban, agricultural, and natural scenarios (Pancorbo et al., 2023; Roth et al., 2012), involves a two-endmember iterative process that add and remove endmembers until the model accuracy no longer improves.

MESMA was executed independently for each of the three levels of detail, using identical settings except for the associated spectral library. For Prato, MESMA was applied to the entire PRISMA hyperspectral image, as the city is centrally located within the captured image frame, allowing for comprehensive modeling. In contrast, for Lucca, only a subset covering approximately one-fourth of the PRISMA image was used due to the city's offset from the frame center, necessitating a mosaicking and clipping process (Section 2.2.1). The MESMA algorithm was implemented using VIPER-Tool v2.1 (Roberts et al., 2019) within ENVI software v5.6.

2.5. Accuracy assessment

The FIs generated by MESMA, representing the fractional abundance of each component within the pixels, were first clipped and co-registered to the respective airborne data footprint. These images were then compared to the airborne-based high-resolution and highly accurate classified map produced using the RF machine learning algorithm (Section 2.2.2). Comparing each pixel from FIs (30 m GSD) with the superimposing group of 10 x 10 classified pixels from airborne reference image (3 m GSD), the per-pixel Bias Error (BE; eq. (2) was calculated for each single class to quantify the difference in estimate LCSM fractional abundance respect the reference data. The per-pixel Absolute Error (AE; eq. (3) was also retrieved as an overall indicator of the total error achieved for each class and, consequently, for the overall result.

$$BiasError(BE) = x - \hat{x} \quad (2)$$

$$AbsoluteError(AE) = |x - \hat{x}| \quad (3)$$

Where x represents the estimated data and $\hat{x}$ the reference data. The BE ranges from −1 (maximum underestimation error) to + 1 (maximum overestimation error), with a value of 0 indicating optimal accuracy (perfect correspondence). The AE ranges from 0 (optimal correspondence) to 1 (worst mismatch). The per-class and overall AE were then computed by averaging the AE values for each class and the total data, respectively.

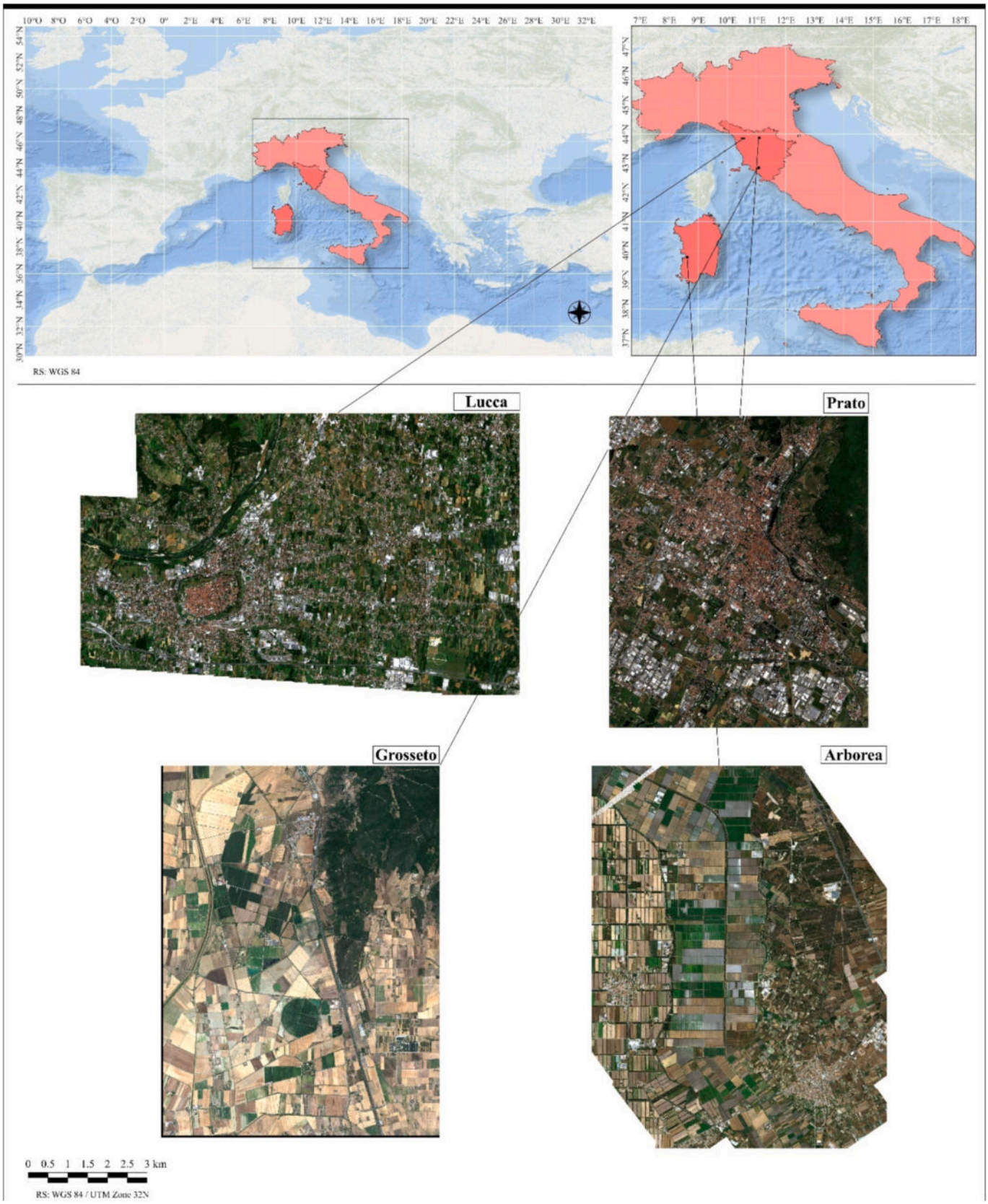

Fig. 1. Location of study areas in a national context (top). The true-color frames (bottom) include the city center, the *peri*-urban belt and the rural landscape of the four study areas.

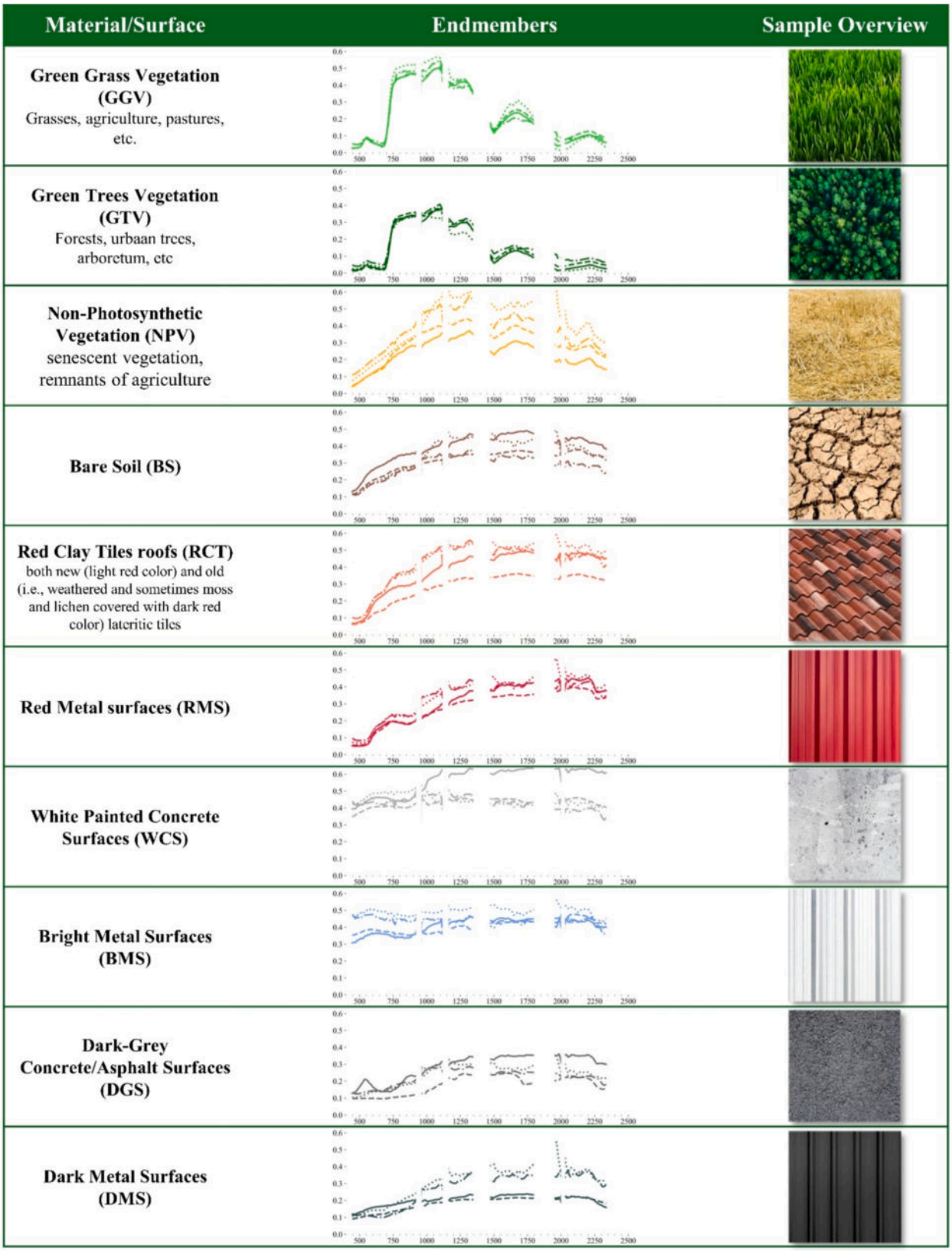

Fig. 2. Definitions of representative land cover and surface material (LCSM) classes for the urban and rural context common to both study areas. The central column shows the stylized mean spectral signature of the endmemembers derived from aerial data (Prato: solid line; Lucca: dashed line; Grosseto: dash-dotted line; Arborea: dotted line).

Table 1
Hierarchical definition of the three detail levels, and respective land cover and surface material (LCSM) classes, tested in MESMA.

Level-1	Level-2	Level-3
Pervious	Green Vegetation (GV)	GGV
		GTV
	NPV	NPV
	BS	BS
Impervious	Red Surfaces (RS)	RCT
		RMS
	Bright-White Surfaces (BWS)	WCS
		BMS
	Dark Surfaces (DS)	DGS
		DMS

3. Results

3.1. Preliminary analysis of endmembers

3.1.1. Number of LCSM classes per PRISMA pixel

The boxplots in Fig. 3 show the distribution of unique airborne-derived LCSM classes within each PRISMA pixel for the four areas (Prato, Lucca, Grosseto, and Arborea), highlighting the mean and median number of classes, ranging from 2 to 5, per pixel. Notably, the number of LCSM classes increases as the complexity of the urban landscape grows (Prato and Lucca). This finding helped to understand class variability and distribution, guiding the selection of 2-, 3-, and 4-endmember models, and corroborating literature-based MESMA model choices basing it on the actual distribution of components in the data.

Spectral distance analysis: inter- and intra-class variability

The inter- and intra-class spectral distances, as quantified by the SAM at different complexity levels, are illustrated in the heatmaps shown in Figs. 4-6. A key observable pattern is the reduced intra-class separability as the complexity level increases from L1 to L2, especially between comparable classes. In L2, it is notable not only how GV is well separated from other classes, with greater separability observed towards the urban-related classes, but also how the separability between other classes becomes less apparent. For example, among the pervious classes, NPV is closer to BS than to GV, while BS shows similarity to RS, which aligns with the spectral signatures observed in Figs. S32-S37. BWS is the most spectrally distinct impervious class, with SAM values ranging from

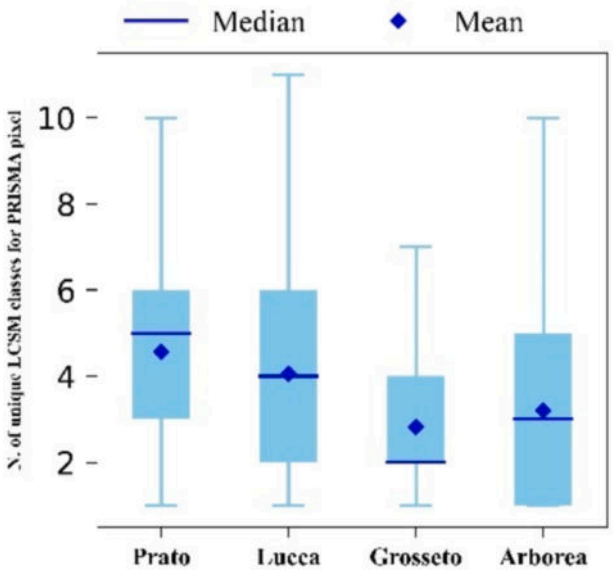

Fig. 3. Boxplots showing the distribution of the number of unique airborne-derived LCSM classes within each PRISMA pixels for the four study areas.

0.33 (BWS-DS in Grosseto) to 0.91 (BWS-GV in Lucca). These patterns are also observed at L3. Indeed, vegetated LCSM classes are closer to one another compared to other classes, particularly the impervious ones. However, at this level of complexity (L3), a certain stabilization in inter- and intra-class distances is evident. That is, in many classes, the gap between intra-class and inter-class separability becomes less pronounced, except for the aforementioned vegetated classes.

3.2. Fraction abundance images

The FIs for each LCSM class, generated by MESMA for all scenes, reveal the macro spatial patterns of structure of the urban and rural landscapes of Prato, Lucca and Grosseto (Figs. 7-12; Figs. S2-S4), even at the coarsest level of detail tested (Level-1). At higher detail levels (Level-2 and Level-3), where the scene was divided into more several LCSM classes (six and ten), a finer representation of the landscape composition is evident for all study areas, despite the limitations of the GSD in capturing detailed object structures.

In Prato, distinct built-up areas are identified, including residential and industrial zones (Figs. 7-9). Residential areas are further differentiated into urban centers and suburban neighborhoods. The urban centers are marked by tightly clustered buildings with traditional RCT, occasionally interrupted by multi-family residential buildings (such as condominiums) with WCS. The suburban residential areas feature more scattered housing with a higher proportion of vegetated areas. The industrial zones, on the other hand, are characterized by large sheds covered in bright metal or white-painted/dark concrete roofs. These built-up districts are densely interconnected with smaller nearby towns and are surrounded by agricultural land.

In Lucca (Figs. 10-12), the urban center is clearly distinguishable, surrounded by the main roads and residential districts arranged in a radial pattern (impervious class). Suburban and *peri*-urban expansion is more pronounced towards the west, marked by a ring of family villas and some industrial structures. Scattered industrial buildings, identified by their BMS or WCS roofs, are also visible throughout the area. Much of the *peri*-urban and rural landscape is composed of permeable surfaces, with dense agricultural fields dominating the scene. Fields covered with harvest residues exhibit a higher concentration of NPV, while other rural fields are characterized by abundant green components, primarily grass. Forested areas are clearly distinguishable, particularly in the northwest near the Serchio River, which also features mixed vegetation along its banks. As is common in agricultural regions, patches of forest are scattered across the rural landscape. Urban vegetation, predominantly trees nestled between buildings and structures, is also clearly detected in the FIs.

Details on Grosseto and Arborea study areas can be observed in Figs. S2-S7 of supplementary material.

3.3. Level-1 accuracy assessment

At Level-1 detail, pervious surfaces were slightly underestimated in Prato and Grosseto, while in Lucca and Arborea they were slightly overestimated, with BE median values of −0.03 (Prato), +0.06 (Lucca), −0.07 (Grosseto) and + 0.01 (Arborea) (Fig. 13). Conversely, the impervious surfaces showed the opposite trend but with better median BE values in Abrborea and Prato (+0.01). Grosseto and Arborea presented a lower BE variability. In Lucca the worst median BE for impervious surfaces was reached with a value of −0.20. The model performed uniformly in Prato and Lucca scenes in terms of overall AE (~ 0.28) (Table 2), with mean values of the individual classes (per-class AE) differing between the two study areas by no more than ± 0.06, respectively. For Grosseto and Arborea lower values were reached (0.125 and 0.088), with a marked equalization between Pervious and Impervious surfaces. The spatial distribution of BE and AE is reported in supplementary materials (Figs. S8-S31).

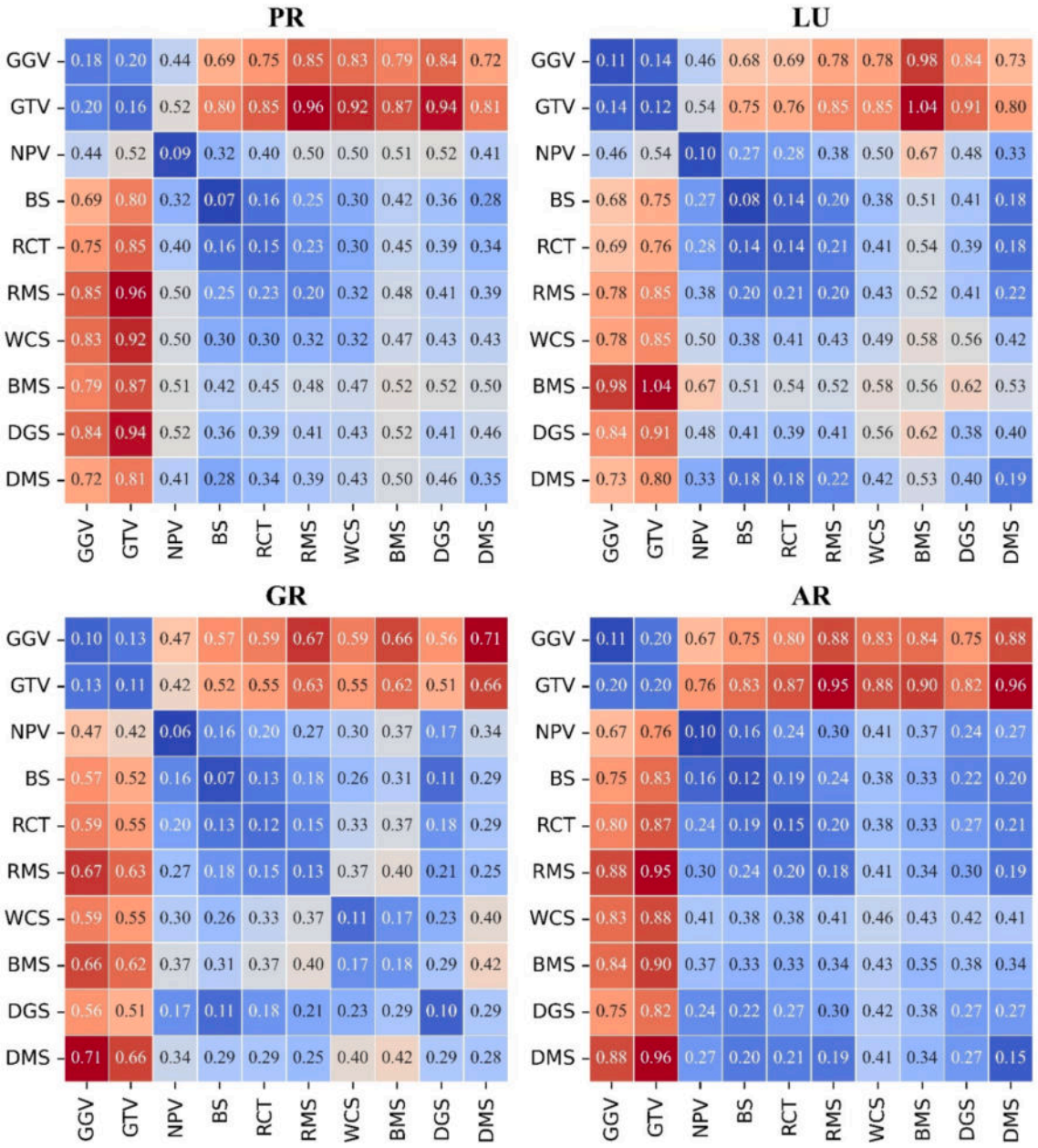

Fig. 4. Heatmaps displaying the mean Spectral Angle Mapper (SAM) values for Level-3. The heatmaps provide a detailed visualization of spectral variability both within (intra-class) and between (inter-class) classes.

3.4. Level-2 accuracy assessment

As the level of detail increased, the AE also rose (Table 2), with BE trends generally diverging from those observed at Level-1 (Fig. 13). At Level-2, BWS resulted the best estimated component in all scenes (Prato, +0.15; Lucca, +0.09; Grosseto, −0.01; Arborea, −0.01). The other classes exhibited varying accuracy between the four study areas. In Prato, RS had the highest AE value (0.336), with the BE displaying a broad distribution across the overestimated error spectrum (median BE = +0.105). In contrast, the DS class, which includes asphalt and concrete, was the most underestimated (median BE = −0.140; AE = 0.293). The median BE for pervious surfaces indicated a general slight underestimation, actually in line with Level-1, with the lowest value found in the NPV class (−0.110). In the other three areas, the BE distribution was more consistent across classes, with median values not dropping below −0.05 (GV, Lucca) and not exceeding + 0.08 (GV, Grosseto). This consistency was also reflected in the per-class AE, with the highest value for GV at 0.235 and 0.234 respectively. The overall AE highest value was at 0.241 (Prato).

The redistribution of negative and positive errors among different classes (false negatives and false positives) can be inferred from the violin-plots shown in Fig. 14 (Level-2) and 15 (Level-3). The plot uses pixels with **B > 0** in a given class as a mask to highlight **BE < 0** in other classes, and vice versa. This approach allows for a comparative analysis of the error patterns across classes by examining how the BE of a specific sign (negative or positive) in one class corresponds to the behavior of BE of opposite sign in all the other classes. In Prato, it is evident that the errors recorded by the GV class are mainly due to confusion with the NPV class, although some of the residuals are also distributed in the other classes. The overestimation errors for the RS and DS classes are systemic, occurring consistently across all other classes. A similar pattern is observed in Lucca, where the systematic nature of the errors is apparent across all classes, reflected in the uniformly lower median error—around 0—found in this study area. Notably, there is a noticeable

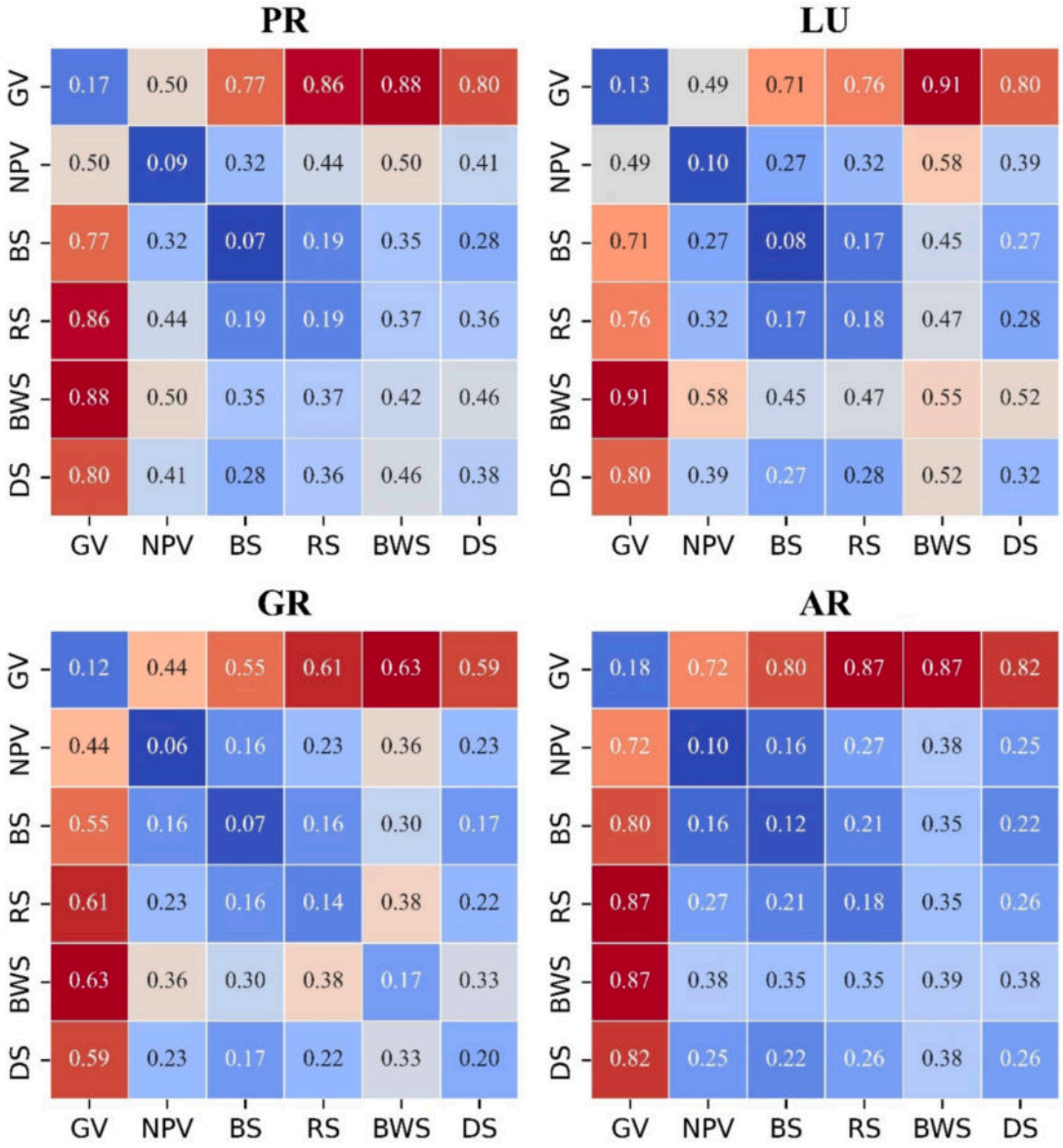

Fig. 5. Heatmaps displaying the mean Spectral Angle Mapper (SAM) values for Level-2. The heatmaps provide a detailed visualization of spectral variability both within (intra-class) and between (inter-class) classes.

interchange of errors between GV and NPV. In Grosseto and Arborea (Fig. 15), GV classes appear to have false positives originating from NPV and BS. Meanwhile, NPV was mainly misclassified as BS in Grosseto and as BS or GV in Arborea. The underestimation of BS contributed to the primary false positives in other classes—meaning that, in most cases, abundances belonging to different categories were mistakenly classified as the BS fraction. Among urban-related LCSMs, DS appears to have absorbed the abundance percentages underestimated for BS (in both Grosseto and Arborea) and GV (in Arborea).

3.5. Level-3 accuracy assessment

At the highest level of detail (Level-3), the accuracy of estimates varied across different classes, particularly those characteristics of urban landscapes. In the Lucca scene, BMS and WCS showed lower mean AE values (ranging from 0.059 to 0.076) and displayed a more contained (close-to-zero) BE distribution. Conversely, the DGS and RCT classes were overestimated and underestimated, respectively, with median BE values of + 0.160 and −0.060. Among the pervious surfaces, is evident as GTV had the highest underprediction (median BE = −0.230), with the worst AE value at this level of detail (0.358). In contrast, GGV was overestimated, with a median BE of + 0.160. In Prato, the results were more varied. Specifically, DGS was the most underpredicted urban surface (median BE = −0.190), whereas WCS were primarily overestimated (median BE = +0.131). DMS, RMS, and BS exhibited notable accuracy, with BE values confined within a narrow range close to −0.01 and AE values of 0.068, 0.078, and 0.062, respectively. The GTV surfaces had a wide BE distribution, indicating a tendency to overestimate, although the median BE remained close to optimal at −0.006. GGV surfaces were generally underestimated, with a median BE of −0.06. In Grosseto and Arborea, worst values for NPV and BS classes were reached (0.355, NPV, Grosseto; 0.250, BS, Grosseto; 0.287, NPV and BS, Arborea).

Observing the error distribution in Prato (Fig. 16), there is a clear and expected interchange between the two GV classes, GGV and GTV, for both negative and positive errors. The underestimation errors in NPV seem to have been misclassified into GTV. The RCT class also appears to have absorbed some NPV errors, but it also exhibits a systemic error, as observed in Level-2, along with DGS and GTV classes. The underestimation errors in the RCT class are primarily due to misclassification with

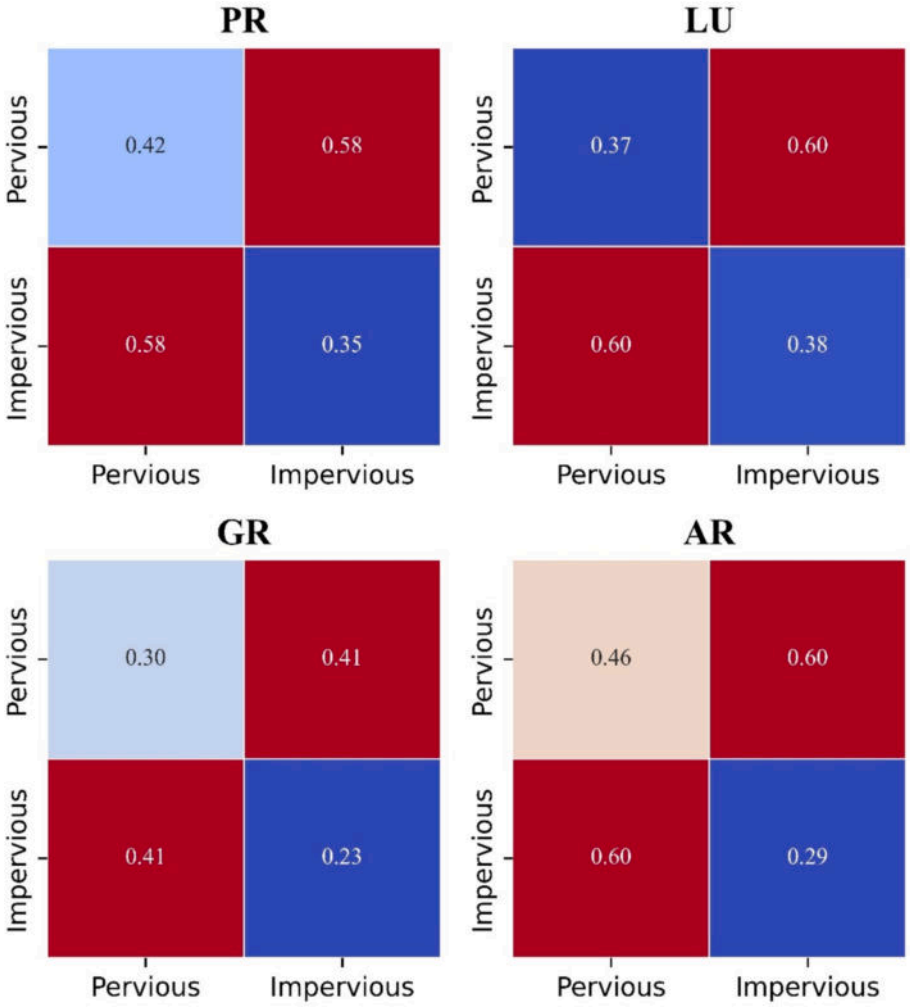

Fig. 6. Heatmaps displaying the mean Spectral Angle Mapper (SAM) values for Level-1. The heatmaps provide a detailed visualization of spectral variability both within (intra-class) and between (inter-class) classes.

the GTV class and with the DGS class. Many of the abundance values in the DGS class seem to have been erroneously attributed to GTV and RCT classes. The RMS class shows expected negative errors due to confusion with RCT, as well as with GTV and DGS. Although white painted, a higher concentration of overestimation errors for WCS appear to arise from concrete/asphalt surfaces (DGS). In Lucca, the error distribution among the Level-3 classes is more uniform, thus more difficult to interpret. There is evident confusion among the three vegetation classes (GGV, GTV, NPV). All the classes seem to share systemic error with GGV. Paradoxically, DGS appears to have been misclassified with various classes, predominantly with pervious surfaces ones. WCS experienced similar misclassification patterns (Fig. 17).

4. Discussions

This study, which marks a pioneering effort to apply the MESMA algorithm to PRISMA HS data for characterizing sub-pixel fractions of urban, *peri*-urban and rural LCSMs, yielded encouraging outcomes in terms of accuracy. Despite the spatial resolution constraints, the overall AE and per-class AE were consistent with existing literature (Clark, 2016; Dennison et al., 2019; Fan and Deng, 2014; Franke et al., 2009), never exceeding 0.282 and 0.336 respectively. For instance, Fan & Deng (2014), employing MESMA with Hyperion HS data (comparable to PRISMA in terms of spectral and spatial resolution) to map urban features, reported RMSE values below 0.2 and a minimum R^2 of 0.7. In Clark et al. (2016) MESMA achieved an overall accuracy below 73.9 % using simulated HyspIRI HS satellite data.

The results reveal that overall and per-class accuracy generally improves as the level of detail increases from Level-1 to Level-2. This may be attributed either to the increased ability to distribute errors across multiple classes or, more plausible, to the limitations of MESMA in managing inter-class similarity (Cao et al., 2022; Degerickx et al., 2019; Petrou and Foschi, 1999). Spectral ambiguity between pervious and impervious surfaces complicates the distinction between these two classes (Weng, 2012), and the similarities observed between NPV, BS, and impervious surfaces such as RCT (Fig. 4) could explain the confusion at Level-1. A decrease in AE value is also observable passing from Level-2 to Level-3 in urbanized areas (Prato and Lucca), which feature a more complex distribution of impervious LCSMs than the rural-specific areas (Grosseto and Arborea), where this AE improvement is less evident. The increased accuracy observed with higher levels of detail contrasts instead with the findings of Franke et al. (2009). However, it is important to note that in their case, lower levels of detail were used as hierarchical spatial constraints for subsequent levels, and higher-resolution aerial HS data were employed instead of spaceborne. This aspect strengthens our approach, as increasing the level of detail will be essential for future analyses where more insight into the complex landscape's composition is required.

Uncertainties in the results can arise from various factors, encouraging further investigation. One key factor is the attributes and origin of the endmembers, along with their number and spatial distribution within the scene, which can significantly impact the accuracy of the sub-

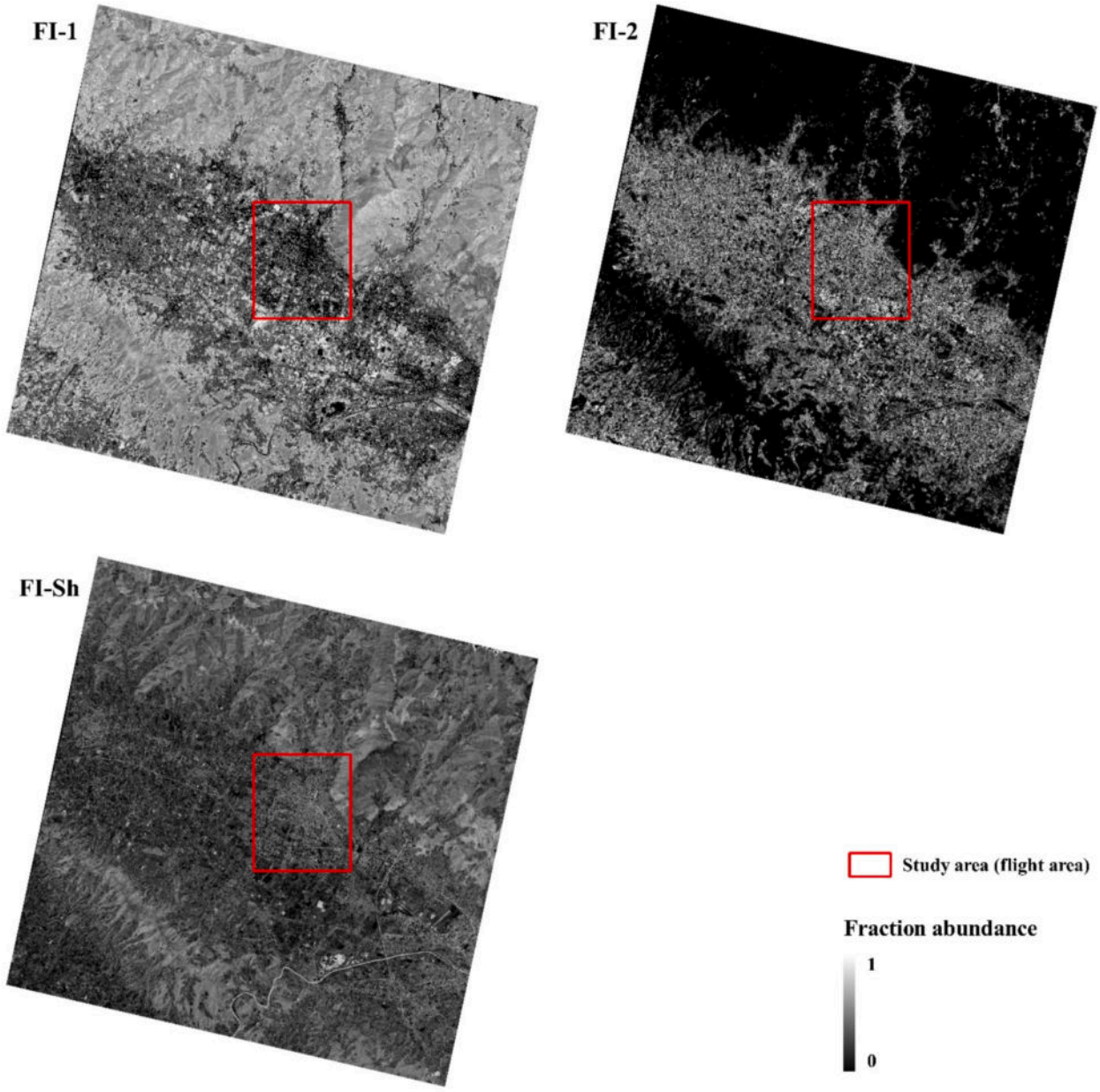

Fig. 7. Fractional abundance images (FIs) of Level-1 for the Prato study area: FI1: Pervious surfaces; FI-2: Impervious surfaces; FI-Sh: Shade fraction.

pixel cover fractions. The distribution and number of endmembers are intended to capture the heterogeneity of pervious and impervious surfaces across the entire image, but this often proves challenging (Somers et al., 2011; Zhang et al., 2019). Scholars generally agree that the optimal configuration involves the minimum number of endmembers necessary to resolve spectral variability (Fan & Deng, 2014; Franke et al., 2009; Roberts et al., 1998; Somers et al., 2011). Both excessive and insufficient numbers of endmembers can lead to residual errors or performance gaps in the model, respectively (Somers et al., 2011). The analyses conducted in this study revealed that, in general, the AE exhibited a lower median as the complexity of the selected models—i.e., the number of endmembers identified by MESMA for a given pixel (2-, 3-, and 4-endmember models)—increased (Figs. S46–S47).

The number of endmembers chosen by MESMA to model each pixel depends on the RMSE threshold. While this study used the default value widely recommended in literature and by the original authors, which ensures reproducibility, we encourage further comparative tests, such as those by Demarchi et al. (2013), to determine an optimal RMSE threshold tailored to specific applications.

Additionally, spectral similarity between cover classes, as well as spectral inter-variability within the same LCSM class (Figs. 4-6) — due to comparable reflectance properties and various physical, chemical, and environmental factors that cause spectral or illumination changes (e.g., species diversity, aging, atmospheric effects, 3D heterogeneity, and non-Lambertian behavior) — pose significant challenges (Cavalli, 2021; Franke et al., 2009; Herold et al., 2004; Herold and Roberts, 2005; van der Linden et al., 2019).

Confusions between roof covers (primarily represented by RCT and WCS) and concrete/asphalted surfaces (DGS) are probably linked to spectral ambiguity (Franke et al., 2009; Herold et al., 2004; Herold and Roberts, 2005). The study area of Prato, particularly the spatial subset involved by aerial flights and thus in the accuracy analysis, predominantly features red roofs texture. This might explain the recurring systemic distribution of the error for this class. More plausible, however, is the confusion between the RCT and BS classes, which can be attributed to the similarity in their spectral signatures (Fig. 2), corroborated by the

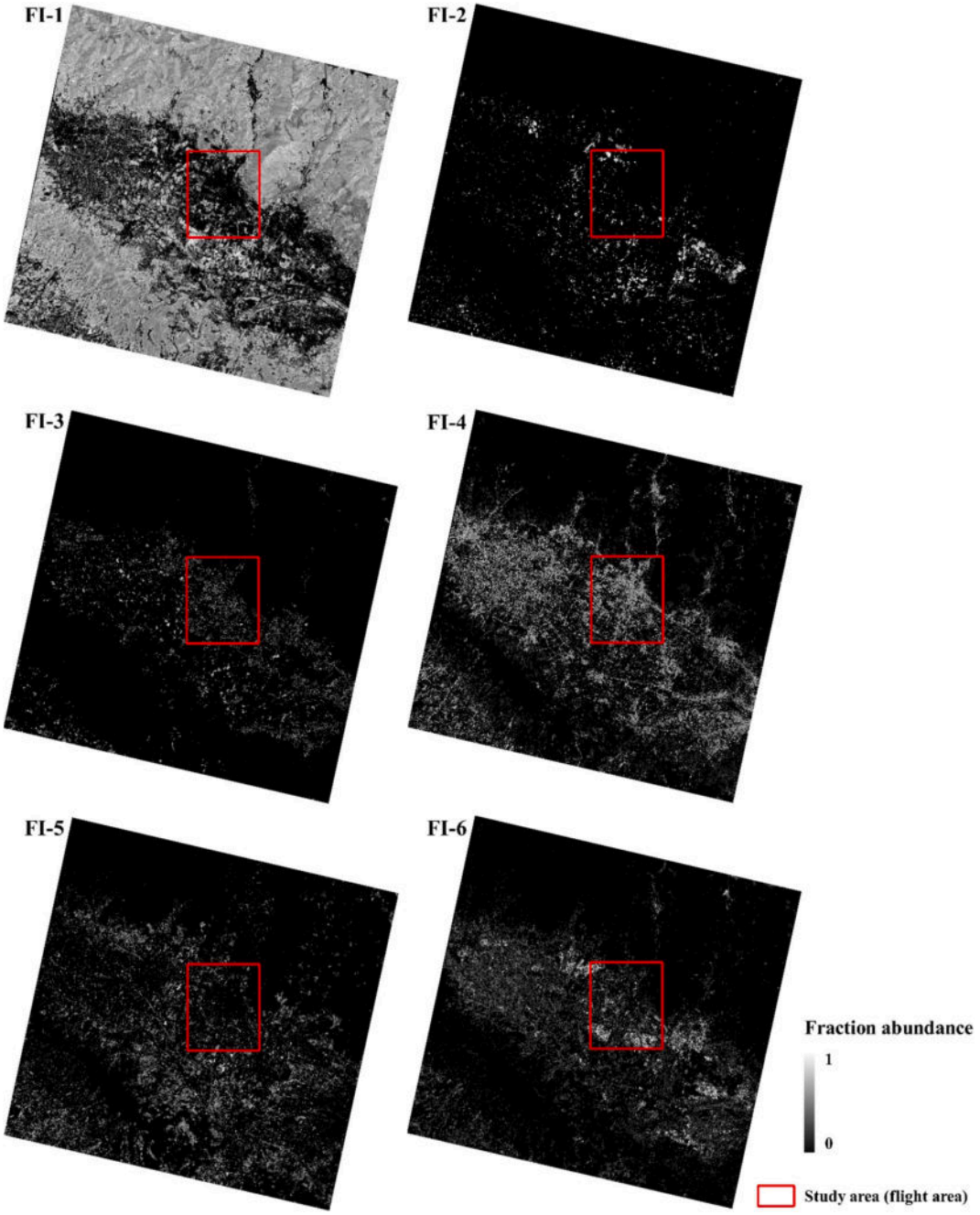

Fig. 8. Fractional abundance images (FIs) of Level-2 for the Prato study area: FI-1: Green Vegetation (GV); FI-2: Non-Photosynthetic Vegetation (NPV); FI-3: Bare Soil (BS); FI-4: Red Surfaces (RS); FI-5: Bright-White Surfaces (BWS); FI-6: Dark Surfaces (DS).

heatmaps (Figs. 4-6). After all, clay is a primary component of soils. Franke et al. (2009) found a significant confusion between red shingle roofs and bare soil. Collinearity between impervious surfaces and soil is a common issue in literature (Demarchi et al., 2012; Feng and Wang, 2018; Xu et al., 2019). Generally, SWIR region is more correlated to the features of man-made artifacts and bare soil (Demarchi et al., 2012). Although PRISMA is one of the few passive imaging spectrometers acquiring high resolution SWIR bands, some spectral faults in this spectrum region were reported (Cogliati et al., 2021; Pepe et al., 2023; Pignatti et al., 2022). Cavalli (2023) recognized that intrinsic feature might affect PRISMA when employed to unmix urban contexts through MESMA, in order of weight: sensor characteristics, processing, geocoding error, and radiometric precision. Errors due to the atmospheric radiometric influence should also be considered (Cavalli, 2021). The FOV and viewing angle are also critical features for HS sensors, as they can be potential sources of brightness and shading artifacts, as well as geometric errors. These aspects should be thoroughly investigated to ensure accurate data collection and analysis (Franke et al., 2009). Since 2023, ASI has limited off-nadir roll angles to $\leq 13°$, but earlier acquisitions allowed greater angles, potentially affecting results (De Luca et al., 2024). In this latter study, in fact, it was observed that geometric errors in PRISMA acquisitions are not spatially uniform and appear to depend on the sensor's geometric features (i.e. off-nadir viewing angle, FOV, orbit) thereby affecting the radiometric and spectral consistency of pixels. However, all these issues will be resolved with the advent of the most updated satellites (PRISMA-2).

The underestimation of urban streets and pavements (mainly represented by DGS), contrasted by an increase in roof classes (e.g., RCT,

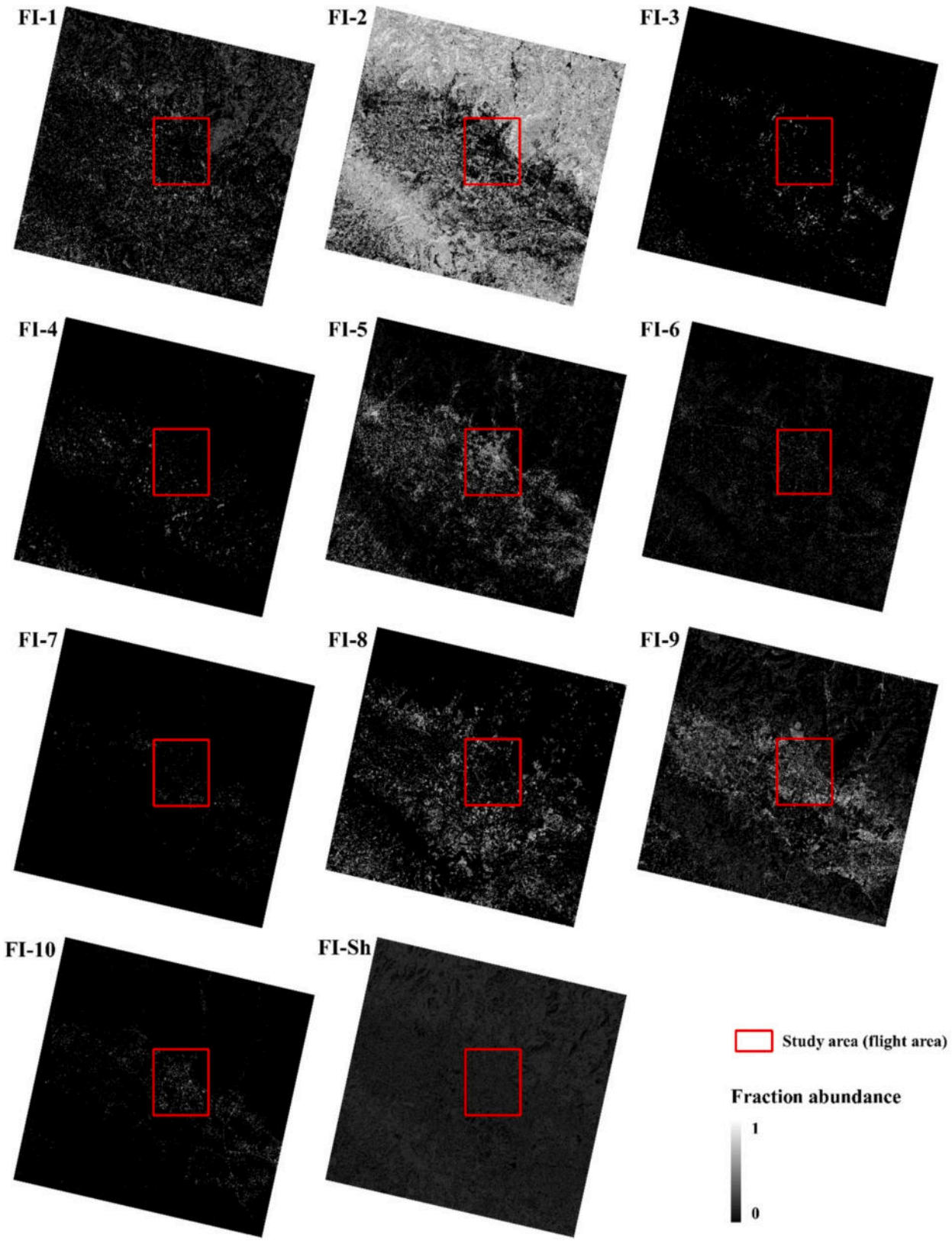

Fig. 9. Fractional abundance images (FIs) of Level-3 for the Prato study area: FI-1: Green Grass Vegetation (GGV); FI-2: Green Tres Vegetation (GTV); FI-3: Non-Photosynthetic Vegetation (NPV); FI-4: Bare Soil (BS); FI-5: Red Clay Tiles (RCT); FI-6: Red Metal Surfaces (RMS); FI-7: White Painted Concrete Surfaces (WCS); FI-8: Bright Metal Surfaces (BMS); FI-9: Dark-Grey Concrete/Asphalt Surfaces (DGS); FI-10: Dark Metal Surfaces (DMS); FI-Sh: Shade fraction.

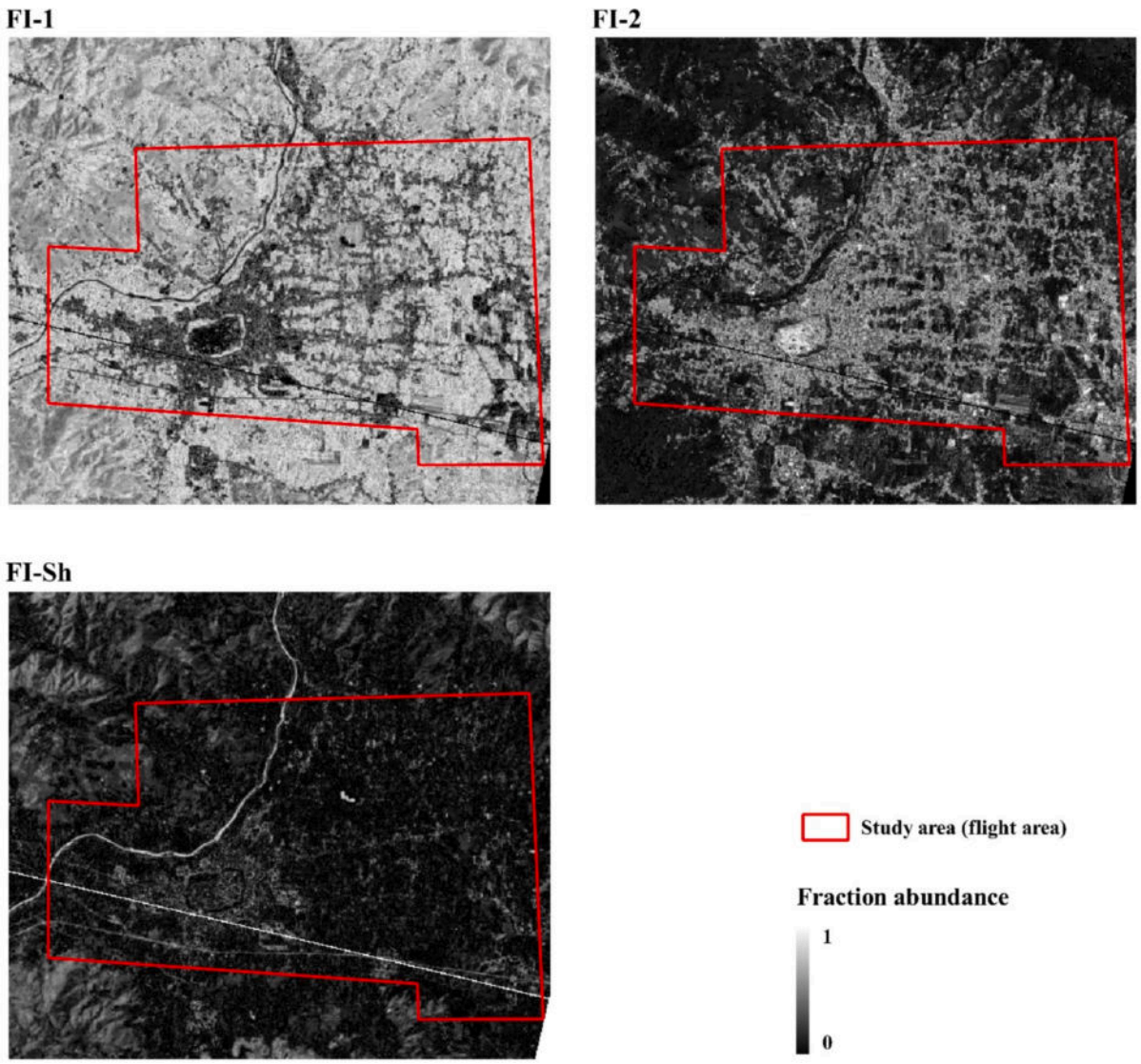

Fig. 10. Fractional abundance images (FIs) of Level-1 for the Lucca study area: FI-1: Pervious surfaces; FI-2: Impervious surfaces; FI-Sh: Shade fraction.

WCS), has been hypothesized by some authors because of the spatial resolution of satellite data. Buildings are often contiguous, frequently shadowing the narrow streets, which are only a few meters wide. For SMA models, resolving high spectral ambiguity present in the spatially complex small objects or linear features becomes challenging at coarse GSDs (Cavalli et al., 2008; van der Linden et al., 2019). Additionally, the spectral separability of asphalt and concrete is significantly hindered by the low reflectance and SNR that these materials exhibit (Cavalli et al., 2008). A feature shared with GTV in the VIS spectral range 400–650 nm (Fig. 2), and which could be the source of that part of the systematic error that has been observed for both two classes. The predominance of green vegetation has already been noted in the literature. Demarchi et al. (2012) observed that when using an RMSE-based model selection method, vegetation endmember-based models were consistently and persistently selected whenever vegetation was present in a mixed pixel. However, these models were also chosen even when vegetation was absent, sometimes leading to the misrepresentation of impervious surfaces.

Among the urban features, metal surfaces were spectrally distinct, as reflected in the low BE values observed at Level 3. Metallic surfaces are particularly influenced by specific light reflection properties, which are more susceptible to variations in the sensor's viewpoint. The BMS classes, in particular, exhibit the highest inter- and intra-class spectral separability among the impervious classes. This factor should be carefully considered when using spectral libraries from different sources. For similar reasons, water bodies were masked in the analysis because preliminary observations of the endmembers indicated that these surfaces are highly sensitive to different camera angles, and their low reflectance can lead to confusion in calculating the shade fraction. It is in fact clearly observable as water bodies highly contributed to shade fraction counting (Figs. 7-12).

Some errors could be attributed to the context in which the materials were positioned. For instance, the underestimation of the RMS in favor of the Pervious might be because most RMSs were in *peri*-urban and rural areas. These are often small roofs with surfaces smaller than the mapping unit (30x30m), leading them to blend with the surrounding vegetation. In urban areas, the same RMSs likely faced confusion with concrete backgrounds, contributing to the observed errors. Franke et al. (2009), in an opposite dynamic, found difficulty isolating tree endmembers in urban environments due to the heterogeneity of background impervious surfaces.

Misclassification between grass and trees was expected, as is a common error documented in the literature (Fan and Deng, 2014; Franke et al., 2009; van der Linden et al., 2019). Errors could potentially be mitigated by identifying different species or at least distinguishing between broadleaf trees and conifers, to reduce spectral ambiguity.

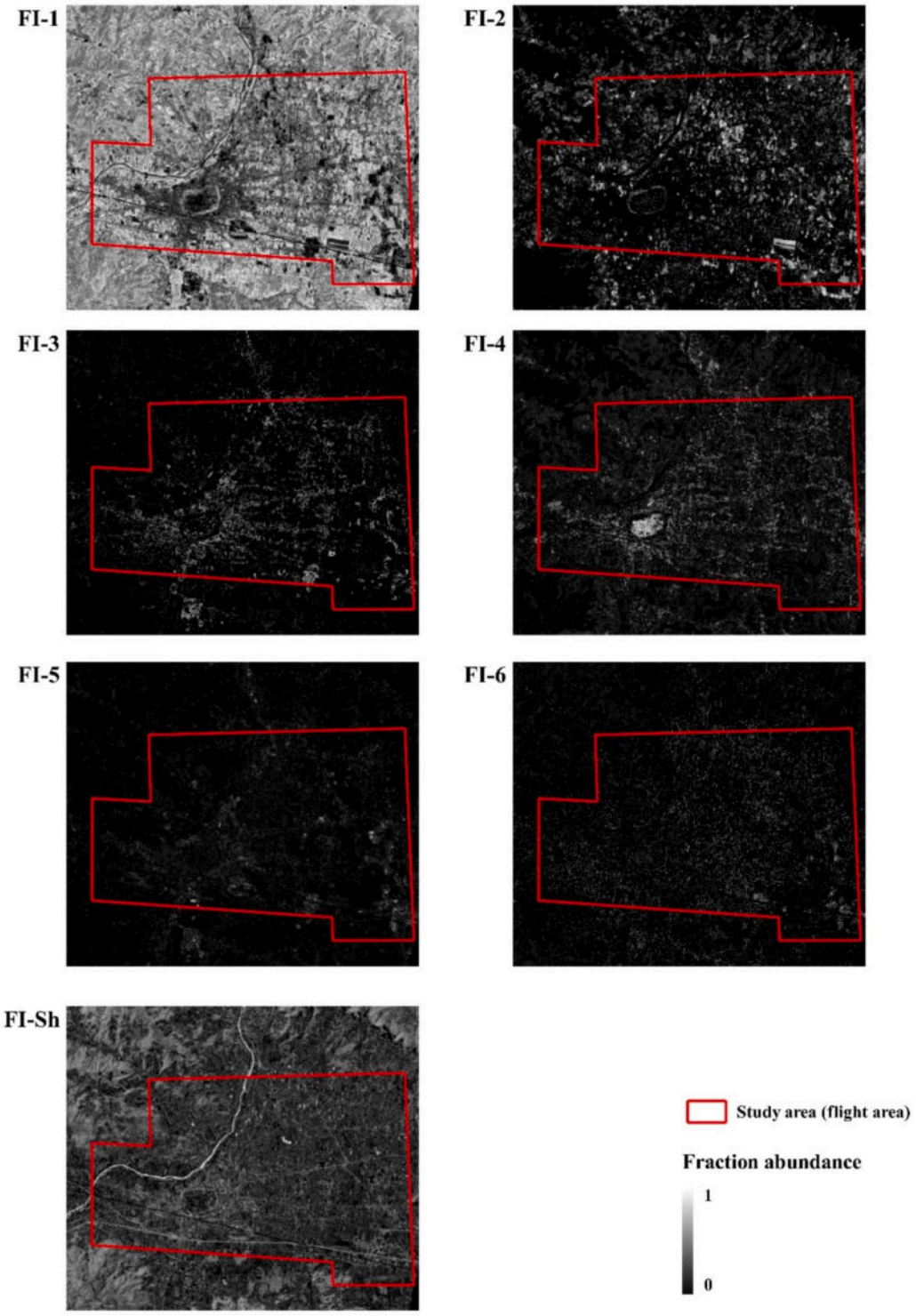

Fig. 11. Fractional abundance images (FIs) of Level-2 for the Lucca study area: FI-1: Green Vegetation (GV); FI-2: Non-Photosynthetic Vegetation (NPV); FI-3: Bare Soil (BS); FI-4: Red Surfaces (RS); FI-5: Bright-White Surfaces (BWS); FI-6: Dark Surfaces (DS); FI-Sh: Shade fraction.

However, this approach requires careful consideration, as the already mentioned sensitivity of MESMA, for inter-class similarity – i.e. when a mixed pixel can be modeled equally well by different endmember models (Degerickx et al., 2019; Petrou and Foschi, 1999).

MESMA managed to model non-photosynthetic vegetation (NPV) fairly well, distinguishing it from green vegetation and soil. The clear spectral differences of photosynthetically active vegetation helped to reduce misclassifications between these classes, but even more notable was the model's performance in distinguishing NPV from bare soil (BS). Distinguishing between NPV and soil is in fact more complex, as it relies on specific absorption features of organic molecules like lignin and cellulose in the SWIR region, varying with soil type, color, and moisture content (Drake et al., 1999; Pancorbo et al., 2023; Pepe et al., 2020; Quintano et al., 2019; Somers et al., 2011).

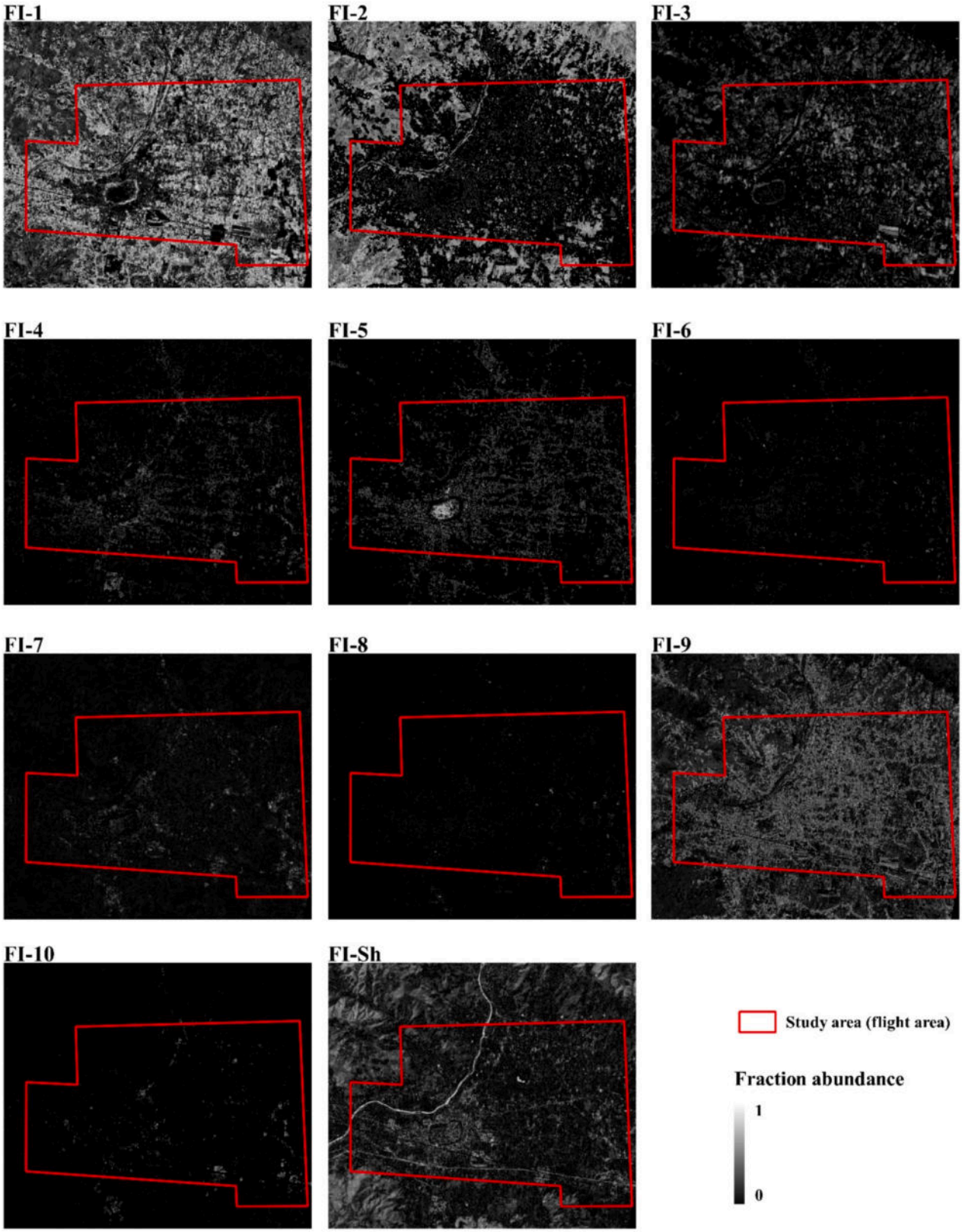

Fig. 12. Fractional abundance images (FIs) of Level-3 for the Lucca study area: Green Grass Vegetation (GGV); FI-2: Green Tres Vegetation (GTV); FI-3: Non-Photosynthetic Vegetation (NPV); FI-4: Bare Soil (BS); FI-5: Red Clay Tiles (RCT); FI-6: Red Metal Surfaces (RMS); FI-7: White Painted Concrete Surfaces (WCS); FI-8: Bright Metal Surfaces (BMS); FI-9: Dark-Grey Concrete/Asphalt Surfaces (DGS); FI-10: Dark Metal Surfaces (DMS); FI-Sh: Shade fraction.

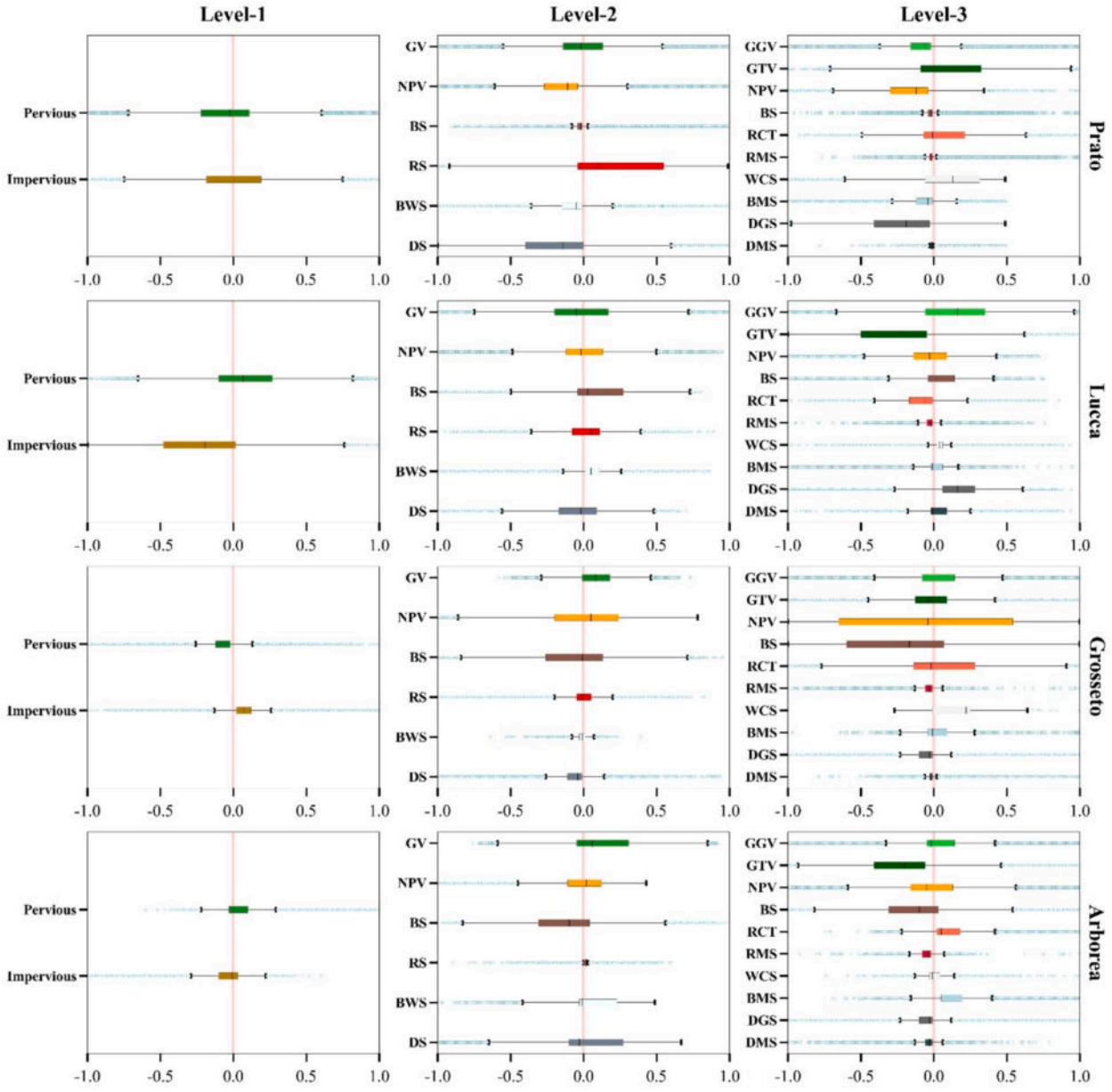

Fig. 13. Bias error (BE) computed for all the classes at each level of detail (left, Level-1; middle, Level-2, right, Level-3).

5. The error report should account for the error propagated by the reference map. Spatial resolution influence

Given pixel size constraints size, achieving a more detailed urban structure remains challenging. Spatial resolution is crucial for accuracy, with higher resolution providing more reliable results than coarser resolutions (Cavalli et al., 2008). Some scholars reported that a minimum spatial resolution of 5 m is necessary to capture urban structures adequately e urban structures (Franke et al., 2009; Small, 2003), noting that even at such resolutions, significant spectral mixing occurs, with single pixels often representing multiple spectral endmembers (van der Linden et al., 2019). In this study, preliminary analyses confirmed that each PRISMA pixel contained, on average, 2 to 5 classes (Fig. 3), with results indicating that the number of LCSM classes increases as the complexity of the urban landscape grows. The contrast between the level of detail captured by airborne data and PRISMA satellite data is visually evident in Figs. S42–S45 of supplementary material, where a comparative overview is provided. This finding further supports the literature's recommendation of using 2- to 4-endmember MESMA models.

However, despite the increase in spectral mixing and loss of spatial detail, the spatial patterns of components were well-preserved across scales. Fractional roofs, vegetation, and soil covers were estimated with reasonable accuracy despite the proven MESMA model's lower performance with 30 m GSD imagery compared to higher-resolution images (van der Linden et al., 2019). The spatial resolution does not seem to have impaired the estimation of details that are commonly difficult to resolve, such as urban vegetation (van der Linden et al., 2019), which was well characterized, as it can be observed in the spatial distribution of BE in Supplementary Material (Figs. S8-S19).

An alternative approach could be to combine increased spatial detail with high spectral information for urban mapping (van der Linden et al., 2019). To leverage the benefits of higher spectral resolution, data fusion techniques are expected to play a crucial role. The same research group has successfully tested a fusion approach using Sentinel-2 multispectral data to enhance the spatial resolution of PRISMA imagery without losing spectral information, applicable to both rural and urban scenarios (De Luca et al., 2024). Future implementations could build on this approach to further refine urban and *peri*-urban composition mapping.

Table 2
Averaged absolute error (AE) for each class (per-class) and for the total data (overall).

Level	Class	PRATO		LUCCA		GROSSETO		ARBOREA	
		AE (per-class)	AE (Overall)	AE (per-class)	AE (Overall)	AE (per-class)	AE (Overall)	AE (per-class)	AE (Overall)
		μ ± σ							
1	***Pervious***	0.274 ± 0.199	0.281 ± 0.283	0.22 ± 0.211	0.282 ± 0.241	0.125 ± 0.137	0.125 ± 0.137	0.098 ± 0.135	0.098 ± 0.135
	Impervious	0.289 ± 0.244		0.333 ± 0.302		0.125 ± 0.137		0.098 ± 0.135	
2	***GV***	0.195 ± 0.199	0.241 ± 0.252	0.235 ± 0.211	0.175 ± 0.167	0.139 ± 0.105	0.188 ± 0.166	0.234 ± 0.212	0.182 ± 0.201
	NPV	0.215 ± 0.244		0.183 ± 0.302		0.251 ± 0.185		0.17 ± 0.176	
	BS	0.225 ± 0.251		0.179 ± 0.174		0.227 ± 0.177		0.241 ± 0.223	
	RS	0.336 ± 0.109		0.137 ± 0.128		0.116 ± 0.146		0.034 ± 0.058	
	BWS	0.152 ± 0.216		0.095 ± 0.136		0.041 ± 0.054		0.149 ± 0.152	
	DS	0.293 ± 0.132		0.183 ± 0.061		0.103 ± 0.142		0.213 ± 0.2	
3	***GGV***	0.169 ± 0.199	0.197 ± 0.219	0.286 ± 0.211	0.188 ± 0.205	0.241 ± 0.307	0.223 ± 0.333	0.189 ± 0.256	0.255 ± 0.256
	GTV	0.258 ± 0.244		0.358 ± 0.302		0.173 ± 0.176		0.283 ± 0.234	
	NPV	0.224 ± 0.251		0.171 ± 0.174		0.356 ± 0.336		0.287 ± 0.300	
	BS	0.062 ± 0.109		0.123 ± 0.128		0.250 ± 0.334		0.287 ± 0.254	
	RCT	0.201 ± 0.216		0.155 ± 0.136		0.297 ± 0.289		0.168 ± 0.255	
	RMS	0.078 ± 0.132		0.054 ± 0.061		0.063 ± 0.108		0.061 ± 0.068	
	WCS	0.227 ± 0.16		0.059 ± 0.072		0.194 ± 0.16		0.072 ± 0.104	
	BMS	0.126 ± 0.157		0.076 ± 0.114		0.105 ± 0.162		0.164 ± 0.181	
	DGS	0.271 ± 0.222		0.211 ± 0.152		0.115 ± 0.179		0.216 ± 0.267	
	DMS	0.068 ± 0.119		0.078 ± 0.112		0.066 ± 0.144		0.055 ± 0.080	

5.1. Airborne reference data and future prospectives

Although using image endmembers can minimize the impact of atmospheric correction (Quintano et al., 2023), identifying a sufficient number of pure pixels for each class at a 30 m GSD is challenging (van der Linden et al., 2019). Field-based spectral libraries are rarely used in urban contexts due to the difficulty of accessing roof surfaces, while laboratory endmembers often lack illumination coherence (De Luca et al., 2023; Somers et al., 2011; Tane et al., 2018). In this study, high spectral and spatial resolution airborne imagery proved to be a valuable alternative for retrieving pure endmembers and validating fraction abundances, fulfilling key criteria for suitable reference data for SMA assessment as defined by Cavalli (2022): i) coverage of most of the study area; ii) higher spatial resolution than target satellite image (ratio between GSDs equal to 10); iii) validation using third-party data; iv) co-registration between reference and target data. This approach is not new, Demarchi et al. (2012) also adopted airborne-derived fraction images in urban environments, but for only validation purposes. Despite the high quality of the classified reference image, any minor errors should still be accounted as a potentially impact factor on the MESMA accuracy estimation.

The proposed strategy offers promising opportunities for future monitoring protocols that leverage high-resolution HS data to collect endmembers in complex landscapes, a prospect that becomes particularly relevant with the growing availability of spaceborne HS missions (e.g., CHIME, SBG, DESIS, EMIT) (Cawse-Nicholson et al., 2021; Green et al., 2021; Qian, 2021). Future research objectives involving HS-equipped UAVs for collecting reference spectra are already planned. This upgrade could significantly enhance environmental analysis by improving pixel purity, because of the very high spatial resolution, along with site-specificity through the UAV's rapid survey capabilities.

However, challenges remain. High-resolution airborne imagery is susceptible to anisotropic and bidirectional reflectance issues, leading to brightness artifacts and shadows. To address this, synergistic corrections will have to be tested, calibrating both UAV and satellite (L2C) data to improve radiometric and spectral alignment. MODTRAN-based ATCOR software, which offers correction tools for satellite, aircraft, and UAV platforms, might be adopted for this purpose.

6. Conclusions

This study highlights the substantial potential of MESMA approach in overcoming the trade-off between spectral and spatial resolution in PRISMA HS data, i.e. effectively mapping the major physical components of urban, *peri*-urban and rural landscapes at a subpixel scale. Although MESMA has been widely used for LCSM estimation, its application to PRISMA HS data remains relatively unexplored. Outcomes showed that accuracy improves as detail (number of classes) increases, while maintaining effective accuracy across all cases. Urbanized areas, as well as surrounding industrial and rural districts, were well represented. Urban vegetation was distinguished in fraction images, although there were notable uncertainties related to the GTV class. Despite some limitations, the average absolute error consistently remained above 75 %. Further investigations into the intrinsic feature of the PRISMA sensor are necessary to understand errors source. However, many of these issues are expected to be addressed with the upcoming PRISMA-2 version.

Future spaceborne HS imaging spectrometers (e.g., CHIME, SBG, DESIS, EMIT) will offer substantial advantages for large-scale studies at consistent temporal frequency with standardized preprocessing. However, the GSD of these missions will be in the same range as PRISMA GSD (30 m), being physically limited by the trade between spatial resolution and radiometric signal-to-noise. Therefore, effectively utilizing these sensors will require substantial efforts to adapt the data for operational applications, especially in complex urban and *peri*-urban environments where significant spectral variation within classes presents unique challenges. The *peri*-urban zone serves as a buffer between urban and natural or semi-natural areas and holds strategic potential as carbon storage hubs through (re)forestation efforts. The MESMA-based approach demonstrated its suitability for supporting urban planners by leveraging spaceborne data to provide quantitative sub-pixel measurements of impervious surfaces, materials, and vegetation abundance – crucial information for subsequent modeling and analysis.

A key aspect of any SMA approach is the selection of representative endmembers. In this study, high-resolution airborne HS pure spectra were effectively utilized to retrieve brightness-coherent endmembers. Future applications will focus on enhancing reference endmember collection using very high-resolution HS-equipped UAVs, improving both spectral purity and ease of sampling.

CRediT authorship contribution statement

Giandomenico De Luca: Writing – review & editing, Writing – original draft, Visualization, Validation, Software, Methodology,

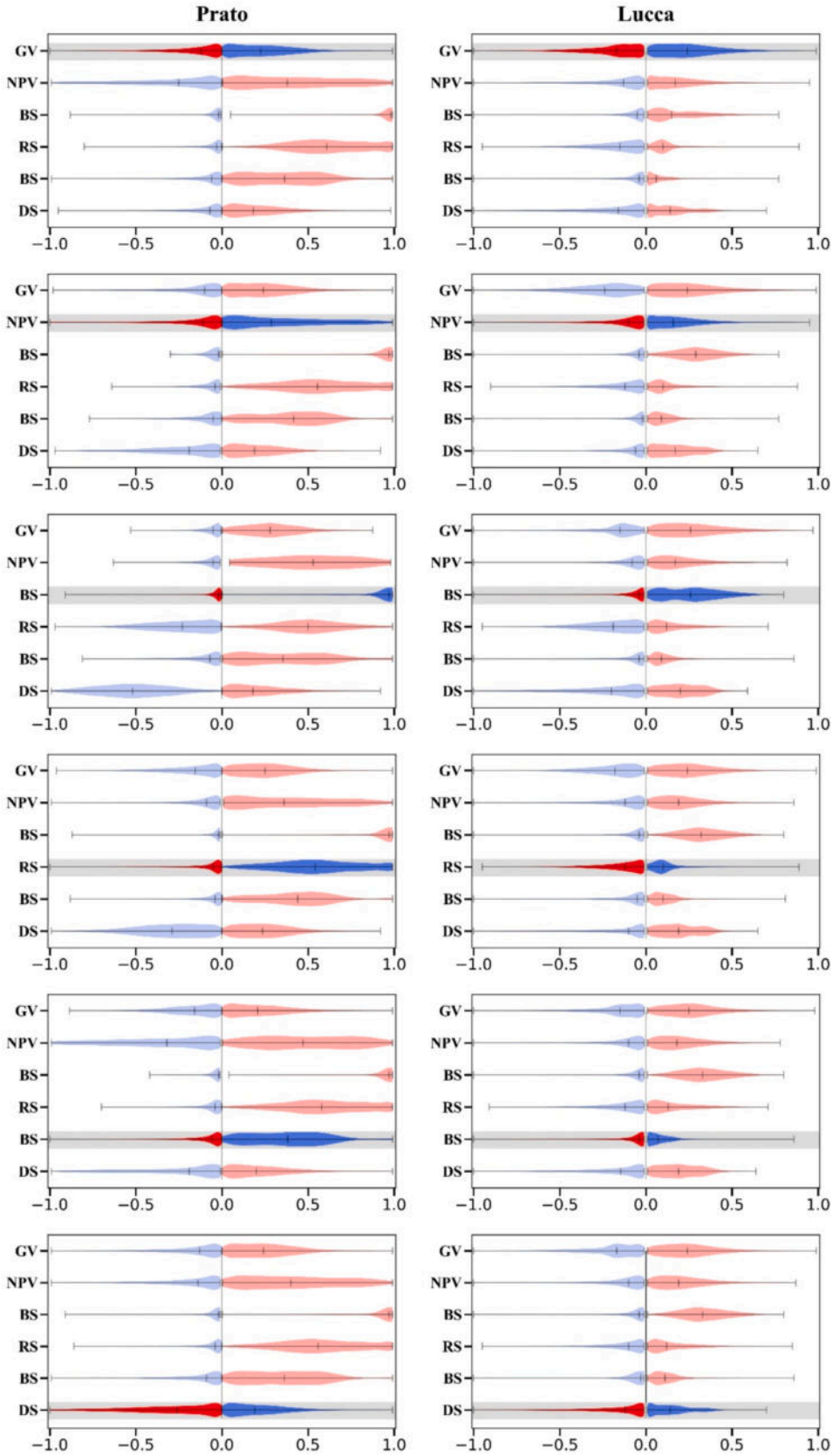

Fig. 14. Error distribution Level-2 (Prato and Lucca). In each subplot, the error distribution for a specific LCSM class is highlighted (gray patch), with positive errors shown in blue and negative errors in red. For that highlighted class, the corresponding pixels with positive errors were used as a mask to select the same pixels in all the other classes, where their corresponding negative errors were plotted (faded blue). Similarly, the pixels with negative errors in the observed class were used as a mask to map the positive errors in all the other classes (faded red).

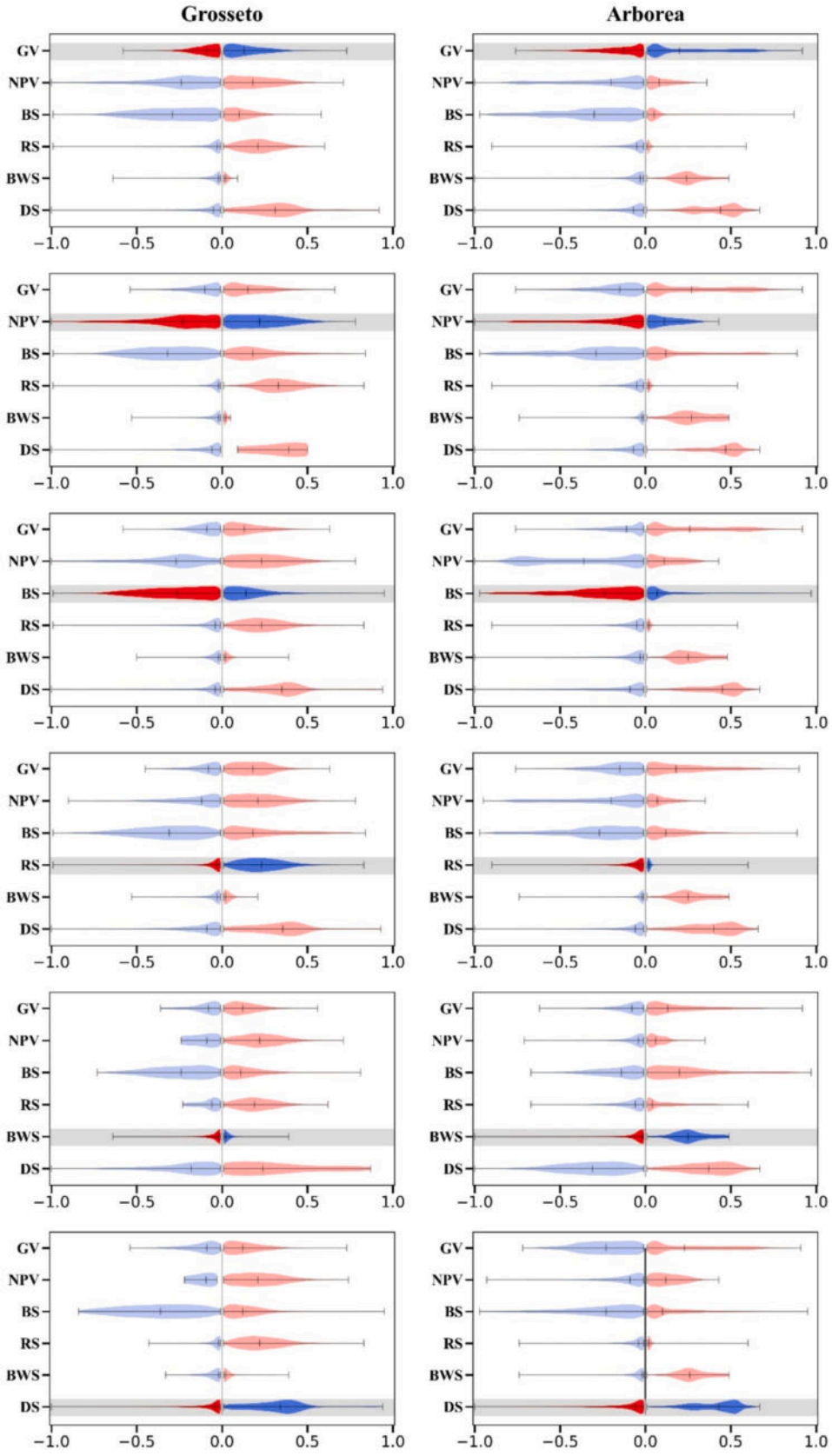

Fig. 15. Error distribution Level-2 (Grosseto and Arborea). In each subplot, the error distribution for a specific LCSM class is highlighted (gray patch), with positive errors shown in blue and negative errors in red. For that highlighted class, the corresponding pixels with positive errors were used as a mask to select the same pixels in all the other classes, where their corresponding negative errors were plotted (faded blue). Similarly, the pixels with negative errors in the observed class were used as a mask to map the positive errors in all the other classes (faded red).

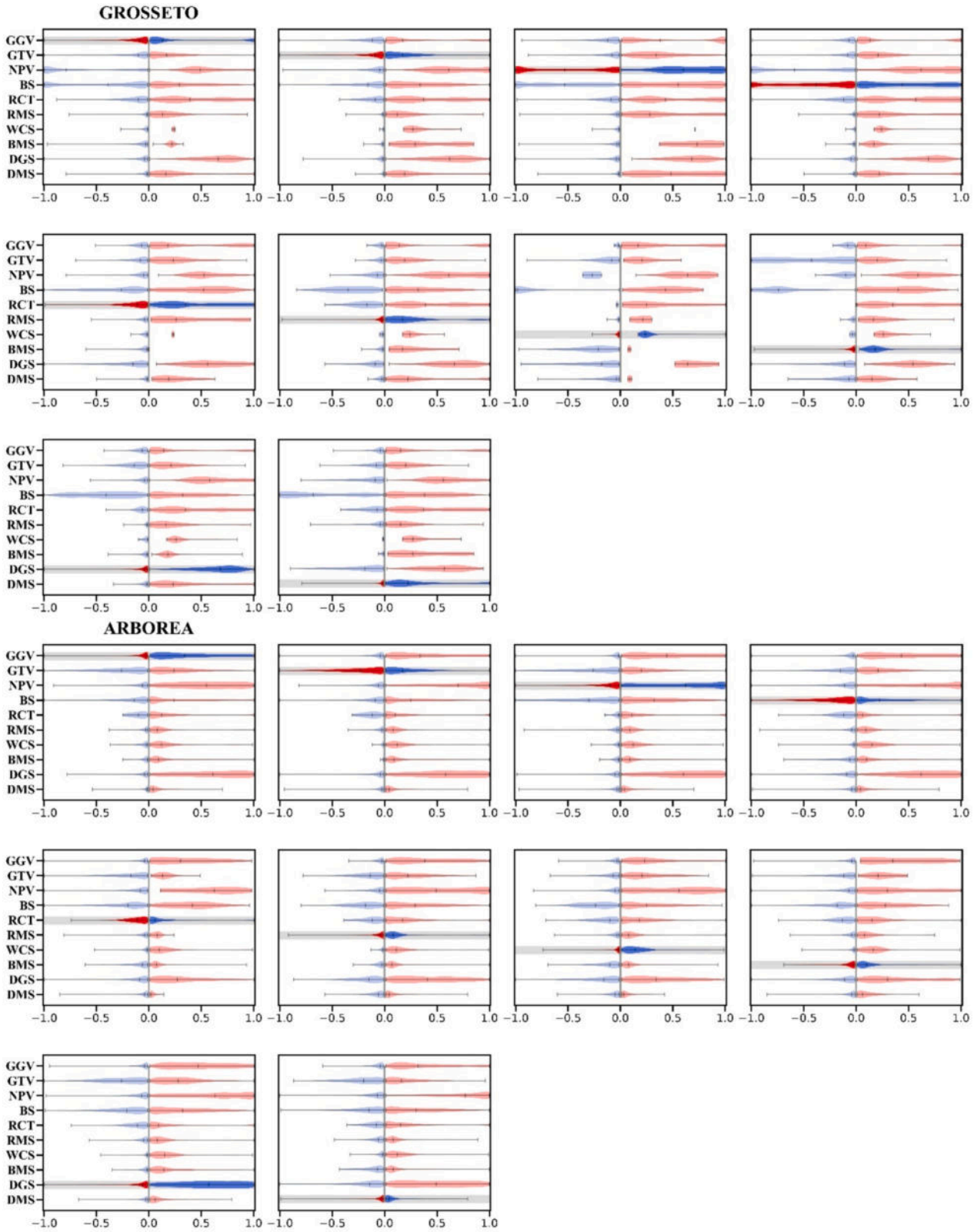

Fig. 16. Error distribution Level-3 (Prato and Lucca). In each subplot, the error distribution for a specific LCSM class is highlighted (gray patch), with positive errors shown in blue and negative errors in red. For that highlighted class, the corresponding pixels with positive errors were used as a mask to select the same pixels in all the other classes, where their corresponding negative errors (faded blue) were plotted. Similarly, the pixels with negative errors in the observed class were used as a mask to map the positive errors (faded red) in all the other classes.

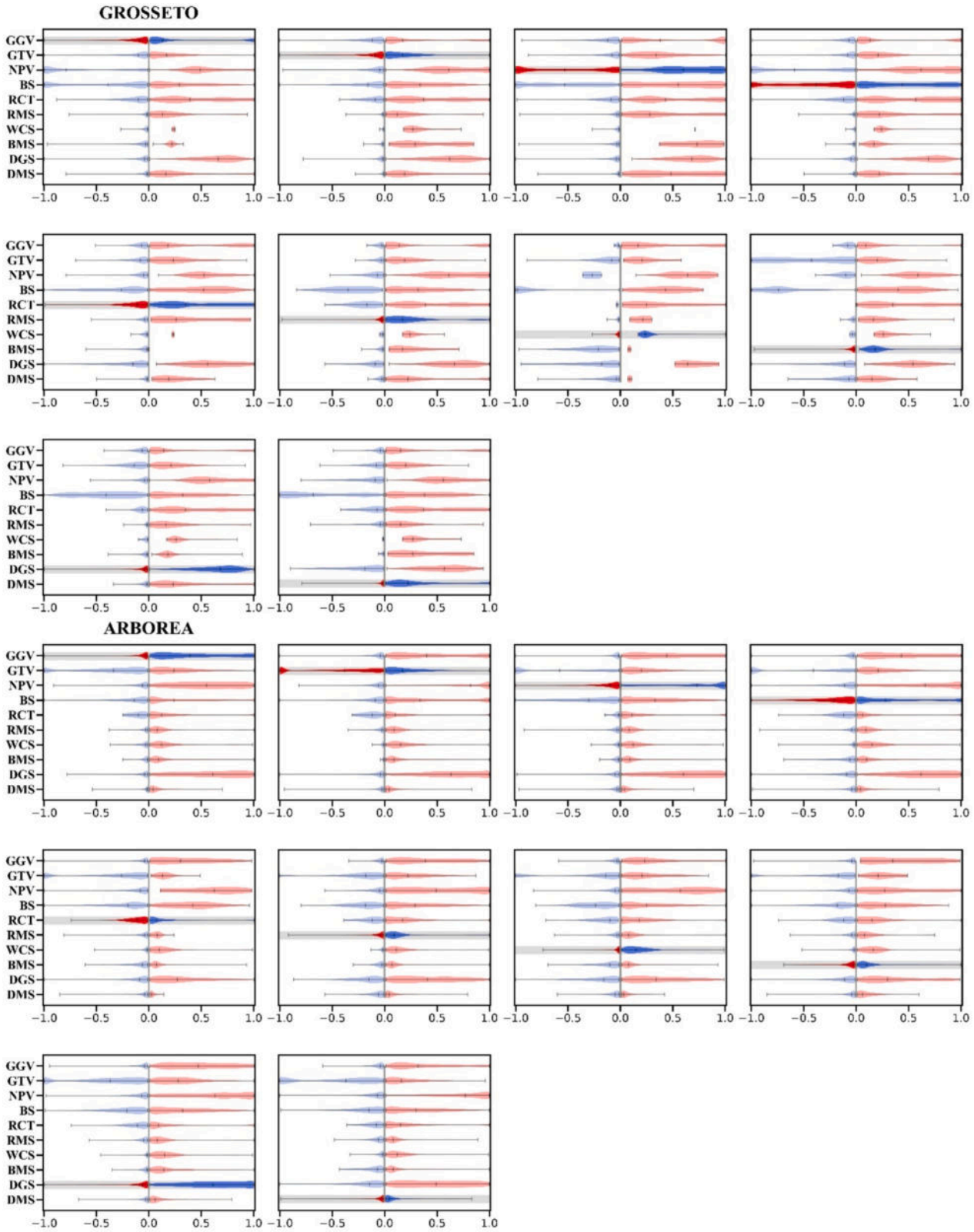

Fig. 17. Error distribution Level-3 (Grosseto and Arborea). In each subplot, the error distribution for a specific LCSM class is highlighted (gray patch), with positive errors shown in blue and negative errors in red. For that highlighted class, the corresponding pixels with positive errors were used as a mask to select the same pixels in all the other classes, where their corresponding negative errors (faded blue) were plotted. Similarly, the pixels with negative errors in the observed class were used as a mask to map the positive errors (faded red) in all the other classes.

Investigation, Formal analysis, Data curation, Conceptualization. **Jose Luis Pancorbo:** Writing – review & editing, Software, Methodology, Investigation, Data curation. **Federico Carotenuto:** Writing – review & editing, Software, Formal analysis, Data curation. **Beniamino Gioli:** Writing – review & editing, Supervision, Resources, Project administration, Funding acquisition. **Giuseppe Modica:** Writing – review & editing, Visualization, Supervision. **Lorenzo Genesio:** Writing – review & editing, Supervision, Resources, Project administration, Funding acquisition.

Declaration of competing interest

The authors declare that they have no known competing financial interests or personal relationships that could have appeared to influence the work reported in this paper.

Acknowledgments

This study made use of PRISMA Products of the Italian Space Agency (ASI), delivered under an ASI License to use, and was made possible by the funding support of the agreement ASI-CNR n. 20195HH0 "Attività scientifica di CAL/VAL della missione PRISMA – PRISCAV". It was also conducted as part of the Italian Integrated Environmental Research Infrastructures System (ITINERIS) project (IR0000032), funded by EU – Next Generation EU PNRR program (M4, C2, I3.1). We thank Ilaria Tabarrani (Tuscany Regional Government) for coordinating the HS flight measurements, and Andrea Genangeli for ground support during the flights. The Level 2 reflectance data obtained with the processing pipeline described in this study are obtainable on request through the Tuscany Regional Government data portal: Prato - https://www502.regione.toscana.it/geonetwork/srv/api/records/r_toscan:4fb45b12-811e-41ed-8c5b-e9531fcc89de#gn-tab-default; Lucca - https://www502.regione.toscana.it/geonetwork/srv/api/records/r_toscan:5b25a427-675d-4143-a595-842c552fd96d.

Appendix A. Supplementary data

Supplementary data to this article can be found online at https://doi.org/10.1016/j.isprsjprs.2025.04.038.

References

Adams, J.B., Smith, M.O., Gillespie, A.R., 1993. Imaging spectroscopy: Interpretation based on spectral mixture analysis. Remote Geochemical Analysis: Elemental and Mineralogical Composition. Topics in Remote Sensing 4, 145–166.

Arcidiaco, L., Corongiu, M., 2025. Analysis of LULC Change Dynamics That Have Occurred in Tuscany (Italy) Since 2007. Land (Basel). https://doi.org/10.3390/land14030443.

Behling, R., Bochow, M., Foerster, S., Roessner, S., Kaufmann, H., 2015. Automated GIS-based derivation of urban ecological indicators using hyperspectral remote sensing and height information. Ecol Indic 48, 218–234. https://doi.org/10.1016/j.ecolind.2014.08.003.

Braga, F., Fabbretto, A., Vanhellemont, Q., Bresciani, M., Giardino, C., Scarpa, G.M., Manfè, G., Concha, J.A., Brando, V.E., 2022. Assessment of PRISMA water reflectance using autonomous hyperspectral radiometry. ISPRS Journal of Photogrammetry and Remote Sensing 192, 99–114. https://doi.org/10.1016/j.isprsjprs.2022.08.009.

Breiman, L., 2001. Random forests. Mach Learn 45, 5–32. https://doi.org/10.1023/A:1010933404324.

Brilli, L., Carotenuto, F., Chiesi, M., Fiorillo, E., Genesio, L., Magno, R., Morabito, M., Nardino, M., Zaldei, A., Gioli, B., 2022. An integrated approach to estimate how much urban afforestation can contribute to move towards carbon neutrality. Science of the Total Environment 842, 156843. https://doi.org/10.1016/j.scitotenv.2022.156843.

Brilli, L., Chiesi, M., Brogi, C., Magno, R., Arcidiaco, L., Bottai, L., Tagliaferri, G., Bindi, M., Maselli, F., 2019. Combination of ground and remote sensing data to assess carbon stock changes in the main urban park of Florence. Urban for Urban Green 43, 126377. https://doi.org/10.1016/j.ufug.2019.126377.

Cao, S., Feng, J., Hu, Z., Li, Q., Wu, G., 2022. Improving estimation of urban land cover fractions with rigorous spatial endmember modeling. ISPRS Journal of Photogrammetry and Remote Sensing 189, 36–49. https://doi.org/10.1016/j.isprsjprs.2022.04.019.

Cavalli, R.M., 2023. The Weight of Hyperion and PRISMA Hyperspectral Sensor Characteristics on Image Capability to Retrieve Urban Surface Materials in the City of Venice. Sensors. https://doi.org/10.3390/s23010454.

Cavalli, R.M., 2022. Spatial Validation of Spectral Unmixing Results: A Case Study of Venice City. Remote Sens (Basel). https://doi.org/10.3390/rs14205165.

Cavalli, R.M., 2021. Capability of Remote Sensing Images to Distinguish the Urban Surface Materials: A Case Study of Venice City. Remote Sens (Basel). https://doi.org/10.3390/rs13193959.

Cavalli, R.M., Fusilli, L., Pascucci, S., Pignatti, S., Santini, F., 2008. Hyperspectral Sensor Data Capability for Retrieving Complex Urban Land Cover in Comparison with Multispectral Data: Venice City Case Study (Italy). Sensors. https://doi.org/10.3390/s8053299.

Cawse-Nicholson, K., Townsend, P.A., Schimel, D., Assiri, A.M., Blake, P.L., Buongiorno, M.F., Campbell, P., Carmon, N., Casey, K.A., Correa-Pabón, R.E., Dahlin, K.M., Dashti, H., Dennison, P.E., Dierssen, H., Erickson, A., Fisher, J.B., Frouin, R., Gatebe, C.K., Gholizadeh, H., Zhang, Q., 2021. NASA's surface biology and geology designated observable: A perspective on surface imaging algorithms. *Remote Sensing of Environment* 257, 112349. https://doi.org/10.1016/j.rse.2021.112349.

Chen, Y., Xu, Y., Zhou, K., 2022. The spatial stress of urban land expansion on the water environment of the Yangtze River Delta in China. Sci Rep 12, 17011. https://doi.org/10.1038/s41598-022-21037-2.

Clark, M.L., 2016. Mapping land cover with hyperspectral and multispectral satellites using machine learning and Spectral Mixture Analysis. In: 2016 IEEE International Geoscience and Remote Sensing Symposium (IGARSS), pp. 513–516. https://doi.org/10.1109/IGARSS.2016.7729127.

Clasen, A., Somers, B., Pipkins, K., Tits, L., Segl, K., Brell, M., Kleinschmit, B., Spengler, D., Lausch, A., Förster, M., 2015. Spectral Unmixing of Forest Crown Components at Close Range, Airborne and Simulated Sentinel-2 and EnMAP Spectral Imaging Scale. Remote Sens (Basel). https://doi.org/10.3390/rs71115361.

Cogliati, S., Sarti, F., Chiarantini, L., Cosi, M., Lorusso, R., Lopinto, E., Miglietta, F., Genesio, L., Guanter, L., Damm, A., Pérez-López, S., Scheffler, D., Tagliabue, G., Panigada, C., Rascher, U., Dowling, T.P.F., Giardino, C., Colombo, R., 2021. The PRISMA imaging spectroscopy mission: overview and first performance analysis. Remote Sens Environ 262, 112499. https://doi.org/10.1016/j.rse.2021.112499.

Damarjati, S., Nugraha, W.A., Arjasakusuma, S., 2022. Mapping the invasive palm species Arenga obtusifolia using multiple endmember spectral mixture analysis (MESMA) and PRISMA hyperspectral data in Ujung Kulon National Park, Indonesia. Geocarto Int 37, 18254–18274. https://doi.org/10.1080/10106049.2022.2138981.

Daughtry, C.S.T., 2001. Discriminating Crop Residues from Soil by Shortwave Infrared Reflectance. Agron J 93, 125–131. https://doi.org/10.2134/agronj2001.931125x.

De Luca, G., Carotenuto, F., Genesio, L., Pepe, M., Toscano, P., Boschetti, M., Miglietta, F., Gioli, B., 2024. Improving PRISMA hyperspectral spatial resolution and geolocation by using Sentinel-2: development and test of an operational procedure in urban and rural areas. ISPRS Journal of Photogrammetry and Remote Sensing 215, 112–135. https://doi.org/10.1016/j.isprsjprs.2024.07.003.

De Luca, G., Modica, G., Silva, J.M.N., Praticò, S., Pereira, J.M.C., 2023. Assessing tree crown fire damage integrating linear spectral mixture analysis and supervised machine learning on Sentinel-2 imagery. Int J Digit Earth 16, 3162–3198. https://doi.org/10.1080/17538947.2023.2243900.

Degerickx, J., Roberts, D.A., Somers, B., 2019. Enhancing the performance of Multiple Endmember Spectral Mixture Analysis (MESMA) for urban land cover mapping using airborne lidar data and band selection. Remote Sens Environ 221, 260–273. https://doi.org/10.1016/j.rse.2018.11.026.

Demarchi, L., Canters, F., Chan, J.-C.-W., Voorde, T. Van de, 2012. Multiple Endmember Unmixing of CHRIS/Proba Imagery for Mapping Impervious Surfaces in Urban and Suburban Environments. IEEE Transactions on Geoscience and Remote Sensing 50, 3409–3424. https://doi.org/10.1109/TGRS.2011.2181853.

Deng, Y., Wu, C., 2016. Development of a Class-Based Multiple Endmember Spectral Mixture Analysis (C-MESMA) Approach for Analyzing Urban Environments. Remote Sens (Basel). https://doi.org/10.3390/rs8040349.

Dennison, P.E., Qi, Y., Meerdink, S.K., Kokaly, R.F., Thompson, D.R., Daughtry, C.S.T., Quemada, M., Roberts, D.A., Gader, P.D., Wetherley, E.B., Numata, I., Roth, K.L., 2019. Comparison of Methods for Modeling Fractional Cover Using Simulated Satellite Hyperspectral Imager Spectra. Remote Sens (Basel). https://doi.org/10.3390/rs11182072.

Dennison, P.E., Roberts, D.A., 2003. Endmember selection for multiple endmember spectral mixture analysis using endmember average RMSE. Remote Sens Environ 87, 123–135. https://doi.org/10.1016/S0034-4257(03)00135-4.

Drake, N.A., Mackin, S., Settle, J.J., 1999. Mapping Vegetation, Soils, and Geology in Semiarid Shrublands Using Spectral Matching and Mixture Modeling of SWIR AVIRIS Imagery. Remote Sens Environ 68, 12–25. https://doi.org/10.1016/S0034-4257(98)00097-2.

Fan, F., Deng, Y., 2014. Enhancing endmember selection in multiple endmember spectral mixture analysis (MESMA) for urban impervious surface area mapping using spectral angle and spectral distance parameters. International Journal of Applied Earth Observation and Geoinformation 33, 290–301. https://doi.org/10.1016/j.jag.2014.06.011.

Feng, B., Wang, J., 2018. Evaluation of Unmixing Methods for Impervious Surface Area Extraction From Simulated EnMAP Imagery. IEEE J Sel Top Appl Earth Obs Remote Sens 11, 1777–1798. https://doi.org/10.1109/JSTARS.2018.2838449.

Fernández-Manso, A., Quintano, C., Fernández-Guisuraga, J.M., Roberts, D., 2024. Next-gen regional fire risk mapping: Integrating hyperspectral imagery and National Forest Inventory data to identify hot-spot wildland-urban interfaces. Science of the Total Environment 940, 173568. https://doi.org/10.1016/j.scitotenv.2024.173568.

Fernandez-Manso, A., Quintano, C., Roberts, D.A., 2016. Burn severity influence on post-fire vegetation cover resilience from Landsat MESMA fraction images time series in Mediterranean forest ecosystems. Remote Sens Environ 184, 112–123. https://doi.org/10.1016/j.rse.2016.06.015.

Franke, J., Roberts, D.A., Halligan, K., Menz, G., 2009. Hierarchical Multiple Endmember Spectral Mixture Analysis (MESMA) of hyperspectral imagery for urban environments. Remote Sens Environ 113, 1712–1723. https://doi.org/10.1016/j.rse.2009.03.018.

García-Pardo, K.A., Moreno-Rangel, D., Domínguez-Amarillo, S., García-Chávez, J.R., 2023. Urban classification of the built-up and seasonal variations in vegetation: A framework integrating multisource datasets. Urban for Urban Green 89, 128114. https://doi.org/10.1016/j.ufug.2023.128114.

García-Pardo, K.A., Moreno-Rangel, D., Domínguez-Amarillo, S., García-Chávez, J.R., 2022. Remote sensing for the assessment of ecosystem services provided by urban vegetation: A review of the methods applied. Urban for Urban Green 74, 127636. https://doi.org/10.1016/j.ufug.2022.127636.

Giardino, C., Bresciani, M., Braga, F., Fabbretto, A., Ghirardi, N., Pepe, M., Gianinetto, M., Colombo, R., Cogliati, S., Ghebrehiwot, S., Laanen, M., Peters, S., Schroeder, T., Concha, J.A., Brando, V.E., 2020. First Evaluation of PRISMA Level 1 Data for Water Applications. Sensors. https://doi.org/10.3390/s20164553.

Green, R.O., Thompson, D.R., EMIT Team, 2021. NASA's Earth Surface Mineral Dust Source Investigation: An Earth Venture Imaging Spectrometer Science Mission. *IEEE International Geoscience and Remote Sensing Symposium IGARSS* 2021, 119–122. https://doi.org/10.1109/IGARSS47720.2021.9554217.

Grimm, N.B., Foster, D., Groffman, P., Grove, J.M., Hopkinson, C.S., Nadelhoffer, K.J., Pataki, D.E., Peters, D.P.C., 2008. The changing landscape: ecosystem responses to urbanization and pollution across climatic and societal gradients. Front Ecol Environ 6, 264–272. https://doi.org/10.1890/070147.

Guarini, R., Loizzo, R., Facchinetti, C., Longo, F., Ponticelli, B., Faraci, M., Dami, M., Cosi, M., Amoruso, L., De Pasquale, V., Taggio, N., 2018. PRISMA hyperspectral mission products. In: IGARSS 2018–2018 IEEE International Geoscience and Remote Sensing Symposium. IEEE, pp. 179–182. https://doi.org/10.1109/IGARSS.2018.8517785.

Herold, M., Roberts, D., 2005. Spectral characteristics of asphalt road aging and deterioration: implications for remote-sensing applications. Appl Opt 44, 4327–4334. https://doi.org/10.1364/AO.44.004327.

Herold, M., Roberts, D.A., Gardner, M.E., Dennison, P.E., 2004. Spectrometry for urban area remote sensing—Development and analysis of a spectral library from 350 to 2400 nm. Remote Sens Environ 91, 304–319. https://doi.org/10.1016/j.rse.2004.02.013.

Huang, C., Zhuang, Q., Meng, X., Zhu, P., Han, J., Huang, L., 2022. A fine spatial resolution modeling of urban carbon emissions: a case study of Shanghai, China. Sci Rep 12, 9255. https://doi.org/10.1038/s41598-022-13487-5.

Kotthaus, S., Smith, T.E.L., Wooster, M.J., Grimmond, C.S.B., 2014. Derivation of an urban materials spectral library through emittance and reflectance spectroscopy. ISPRS Journal of Photogrammetry and Remote Sensing 94, 194–212. https://doi.org/10.1016/j.isprsjprs.2014.05.005.

Loizzo, R., Daraio, M., Guarini, R., Longo, F., Lorusso, R., Dini, L., Lopinto, E., 2019. Prisma Mission Status and Perspective. In: IGARSS 2019–2019 IEEE International Geoscience and Remote Sensing Symposium, pp. 4503–4506. https://doi.org/10.1109/IGARSS.2019.8899272.

Lumia, G., Praticò, S., Di Fazio, S., Cushman, S., Modica, G., 2023. Combined use of urban Atlas and Corine land cover datasets for the implementation of an ecological network using graph theory within a multi-species approach. Ecol Indic 148, 110150. https://doi.org/10.1016/j.ecolind.2023.110150.

Luti, T., De Fioravante, P., Marinosci, I., Strollo, A., Riitano, N., Falanga, V., Mariani, L., Congedo, L., Munafò, M., 2021. Land Consumption Monitoring with SAR Data and Multispectral Indices. Remote Sens (Basel). https://doi.org/10.3390/rs13081586.

McDonald, R.I., Marcotullio, P.J., Güneralp, B., 2013. Urbanization and Global Trends in Biodiversity and Ecosystem Services BT - Urbanization, Biodiversity and Ecosystem Services: Challenges and Opportunities: A Global Assessment. In: Elmqvist, T., Fragkias, M., Goodness, J., Güneralp, B., Marcotullio, P.J., McDonald, R.I., Parnell, S., Schewenius, M., Sendstad, M., Seto, K.C., Wilkinson, C. (Eds.), Urbanization, Biodiversity and Ecosystem Services: Challenges and Opportunities. Springer Netherlands, Dordrecht, pp. 31–52. https://doi.org/10.1007/978-94-007-7088-1_3.

McPhearson, T., Haase, D., Kabisch, N., Gren, Å., 2016. Advancing understanding of the complex nature of urban systems. Ecol Indic 70, 566–573. https://doi.org/10.1016/j.ecolind.2016.03.054.

Meerdink, S.K., Roberts, D.A., Roth, K.L., King, J.Y., Gader, P.D., Koltunov, A., 2019. Classifying California plant species temporally using airborne hyperspectral imagery. Remote Sens Environ 232, 111308. https://doi.org/10.1016/j.rse.2019.111308.

Müller, N., Ignatieva, M., Nilon, C.H., Werner, P., Zipperer, W.C., 2013. Patterns and Trends in Urban Biodiversity and Landscape Design BT - Urbanization, Biodiversity and Ecosystem Services: Challenges and Opportunities: A Global Assessment. In: Elmqvist, T., Fragkias, M., Goodness, J., Güneralp, B., Marcotullio, P.J., McDonald, R.I., Parnell, S., Schewenius, M., Sendstad, M., Seto, K.C., Wilkinson, C. (Eds.), Urbanization, Biodiversity and Ecosystem Services: Challenges and Opportunities. Springer Netherlands, Dordrecht, pp. 123–174. https://doi.org/10.1007/978-94-007-7088-1_10.

Mulya, S.P., Putro, H.P.H., Hudalah, D., 2023. Review of peri-urban agriculture as a regional ecosystem service. Geography and Sustainability 4, 244–254. https://doi.org/10.1016/j.geosus.2023.06.001.

Neyns, R., Canters, F., 2022. Mapping of Urban Vegetation with High-Resolution Remote Sensing: A Review. Remote Sens (Basel). https://doi.org/10.3390/rs14041031.

OrfeoToolBox - OTB, 2024. EdgeExtraction. URL https://www.orfeo-toolbox.org/CookBook/Applications/app_EdgeExtraction.html. Accessed: February 2025.

Pancorbo, J.L., Carotenuto, F., De De Luca, G., Genesio, L., Gioli, B., 2024. Thermal and Radiative Properties of Photovoltaic, Artificial and Natural Land Covers to Support Urban Planning. In: IGARSS 2024–2024 IEEE International Geoscience and Remote Sensing Symposium, pp. 1151–1155. https://doi.org/10.1109/IGARSS53475.2024.10642148.

Pancorbo, J.L., Quemada, M., Roberts, D.A., 2023. Drought impact on cropland use monitored with AVIRIS imagery in Central Valley, California. Science of the Total Environment 859, 160198. https://doi.org/10.1016/j.scitotenv.2022.160198.

Pedregosa, F., Varoquaux, G., Gramfort, A., Michel, V., Thirion, B., Grisel, O., Blondel, M., Prettenhofer, P., Weiss, R., Dubourg, V., Vanderplas, J., Passos, A., Cournapeau, D., Brucher, M., Perrot, M., Duchesnay, É., 2011. Scikit-learn: Machine learning in Python. Journal of Machine Learning Research 12, 2825–2830.

Pepe, M., Pompilio, L., Gioli, B., Busetto, L., Boschetti, M., 2020. Detection and Classification of Non-Photosynthetic Vegetation from PRISMA Hyperspectral Data in Croplands. Remote Sens (Basel). https://doi.org/10.3390/rs12233903.

Pepe, M., Pompilio, L., Ranghetti, L., Nutini, F., Boschetti, M., 2023. Mapping spatial distribution of crop residues using PRISMA satellite imaging spectroscopy. Eur J Remote Sens 56, 2122872. https://doi.org/10.1080/22797254.2022.2122872.

Petrou, M., Foschi, P.G., 1999. Confidence in linear spectral unmixing of single pixels. IEEE Transactions on Geoscience and Remote Sensing 37, 624–626. https://doi.org/10.1109/36.739132.

Pignatti, S., Amodeo, A., Carfora, M.F., Casa, R., Mona, L., Palombo, A., Pascucci, S., Rosoldi, M., Santini, F., Laneve, G., 2022. PRISMA L1 and L2 Performances within the PRISCAV Project: The Pignola Test Site in Southern Italy. Remote Sens (Basel) 14. https://doi.org/10.3390/rs14091985.

Pignatti, S., Palombo, A., Pascucci, S., Romano, F., Santini, F., Simoniello, T., Umberto, A., Vincenzo, C., Acito, N., Diani, M., Matteoli, S., Corsini, G., Casa, R., Bonis, R. De, Laneve, G., Ananasso, C., 2013. The PRISMA hyperspectral mission: Science activities and opportunities for agriculture and land monitoring. In: 2013 IEEE International Geoscience and Remote Sensing Symposium - IGARSS, pp. 4558–4561. https://doi.org/10.1109/IGARSS.2013.6723850.

Powell, R.L., Roberts, D.A., 2008. Characterizing Variability of the Urban Physical Environment for a Suite of Cities in Rondônia, Brazil. Earth Interact 12, 1–32. https://doi.org/10.1175/2008EI246.1.

Qian, S.-E., 2021. Hyperspectral Satellites, Evolution, and Development History. IEEE J Sel Top Appl Earth Obs Remote Sens 14, 7032–7056. https://doi.org/10.1109/JSTARS.2021.3090256.

Quintano, C., Calvo, L., Fernández-Manso, A., Suárez-Seoane, S., Fernandes, P.M., Fernández-Guisuraga, J.M., 2023. First evaluation of fire severity retrieval from PRISMA hyperspectral data. Remote Sens Environ 295, 113670. https://doi.org/10.1016/j.rse.2023.113670.

Quintano, C., Fernández-Manso, A., Calvo, L., Roberts, D.A., 2019. Vegetation and Soil Fire Damage Analysis Based on Species Distribution Modeling Trained with Multispectral Satellite Data. Remote Sens (Basel). https://doi.org/10.3390/rs11151832.

Quintano, C., Fernández-Manso, A., Roberts, D.A., 2020. Enhanced burn severity estimation using fine resolution ET and MESMA fraction images with machine learning algorithm. Remote Sens Environ 244, 111815. https://doi.org/10.1016/j.rse.2020.111815.

Quintano, C., Fernandez-Manso, A., Roberts, D.A., 2017. Burn severity mapping from Landsat MESMA fraction images and Land Surface Temperature. Remote Sens Environ 190, 83–95. https://doi.org/10.1016/j.rse.2016.12.009.

Roberts, D.A., Gardner, M., Church, R., Ustin, S., Scheer, G., Green, R.O., 1998. Mapping Chaparral in the Santa Monica Mountains Using Multiple Endmember Spectral Mixture Models. Remote Sens Environ 65, 267–279. https://doi.org/10.1016/S0034-4257(98)00037-6.

Roberts, D.A., Halligan, K., Dennison, P., Dudley, K., Somers, B., Crabbé, A., 2019. VIPER Tools User Manual Version 2.1.

Roberts, D.A., Quattrochi, D.A., Hulley, G.C., Hook, S.J., Green, R.O., 2012. Synergies between VSWIR and TIR data for the urban environment: An evaluation of the potential for the Hyperspectral Infrared Imager (HyspIRI) Decadal Survey mission. Remote Sens Environ 117, 83–101. https://doi.org/10.1016/j.rse.2011.07.021.

Roth, K.L., Dennison, P.E., Roberts, D.A., 2012. Comparing endmember selection techniques for accurate mapping of plant species and land cover using imaging spectrometer data. Remote Sens Environ 127, 139–152. https://doi.org/10.1016/j.rse.2012.08.030.

Schaaf, A.N., Dennison, P.E., Fryer, G.K., Roth, K.L., Roberts, D.A., 2011. Mapping Plant Functional Types at Multiple Spatial Resolutions Using Imaging Spectrometer Data. Gisci Remote Sens 48, 324–344. https://doi.org/10.2747/1548-1603.48.3.324.

Scheffler, D., Hollstein, A., Diedrich, H., Segl, K., Hostert, P., 2017. AROSICS: An Automated and Robust Open-Source Image Co-Registration Software for Multi-Sensor Satellite Data. Remote Sens (Basel). https://doi.org/10.3390/rs9070676.

Shimabukuro, Y.E., Ponzoni, F.J., 2018. Spectral mixture for remote sensing: Linear model and applications. Springer. https://doi.org/10.1007/978-3-030-02017-0.

Small, C., 2005. A global analysis of urban reflectance. Int J Remote Sens 26, 661–681. https://doi.org/10.1080/01431160310001654950.

Small, C., 2003. High spatial resolution spectral mixture analysis of urban reflectance. Remote Sens Environ 88, 170–186. https://doi.org/10.1016/j.rse.2003.04.008.

Somers, B., Asner, G.P., Tits, L., Coppin, P., 2011. Endmember variability in Spectral Mixture Analysis: A review. Remote Sens Environ 115, 1603–1616. https://doi.org/10.1016/j.rse.2011.03.003.

Tane, Z., Roberts, D., Veraverbeke, S., Casas, Á., Ramirez, C., Ustin, S., 2018. Evaluating Endmember and Band Selection Techniques for Multiple Endmember Spectral

Mixture Analysis using Post-Fire Imaging Spectroscopy. Remote Sens (Basel). https://doi.org/10.3390/rs10030389.
van der Linden, S., Okujeni, A., Canters, F., Degerickx, J., Heiden, U., Hostert, P., Priem, F., Somers, B., Thiel, F., 2019. Imaging Spectroscopy of Urban Environments. Surv Geophys 40, 471–488. https://doi.org/10.1007/s10712-018-9486-y.
Vavassori, A., Giuliani, G., Brovelli, M.A., 2023. Mapping Local Climate Zones in Lausanne (Switzerland) with Sentinel-2 and PRISMA imagery: comparison of classification performance using different band combinations and building height data. Int J Digit Earth 16, 4790–4810. https://doi.org/10.1080/17538947.2023.2283485.
Veraverbeke, S., Somers, B., Gitas, I., Katagis, T., Polychronaki, A., Goossens, R., 2012. Spectral mixture analysis to assess post-fire vegetation regeneration using Landsat Thematic Mapper imagery: Accounting for soil brightness variation. International Journal of Applied Earth Observation and Geoinformation 14, 1–11. https://doi.org/10.1016/j.jag.2011.08.004.
Wang, Y., Zhang, X., Xu, J., Pan, G., Zhao, Y., Liu, Y., Liu, H., Liu, J., 2022. Accumulated impacts of imperviousness on surface and subsurface hydrology—continuous modelling at urban street block scale. J Hydrol (Amst) 608, 127621. https://doi.org/10.1016/j.jhydrol.2022.127621.
Weng, Q., 2012. Remote sensing of impervious surfaces in the urban areas: Requirements, methods, and trends. Remote Sens Environ 117, 34–49. https://doi.org/10.1016/j.rse.2011.02.030.
Weng, Q., Hu, X., Lu, D., 2008. Extracting impervious surfaces from medium spatial resolution multispectral and hyperspectral imagery: a comparison. Int J Remote Sens 29, 3209–3232. https://doi.org/10.1080/01431160701469024.
Wu, C., Deng, C., Jia, X., 2014. Spatially Constrained Multiple Endmember Spectral Mixture Analysis for Quantifying Subpixel Urban Impervious Surfaces. IEEE J Sel Top Appl Earth Obs Remote Sens 7, 1976–1984. https://doi.org/10.1109/JSTARS.2014.2318018.
Wu, H., Huang, B., Zheng, Z., Ma, Z., Zeng, Y., 2022. Spatial Heterogeneity and Temporal Variation in Urban Surface Albedo Detected by High-Resolution Satellite Data. Remote Sens (Basel). https://doi.org/10.3390/rs14236166.
Xu, F., Cao, X., Chen, X., Somers, B., 2019. Mapping impervious surface fractions using automated Fisher transformed unmixing. Remote Sens Environ 232, 111311. https://doi.org/10.1016/j.rse.2019.111311.
Yokoya, N., Grohnfeldt, C., Chanussot, J., 2017. Hyperspectral and Multispectral Data Fusion: A comparative review. IEEE Geosci Remote Sens Mag 5, 29–56. https://doi.org/10.1109/MGRS.2016.2637824.
Yuhas, R.H., Goetz, A.F., Boardman, J.W., 1992. Discrimination among semi-arid landscape endmembers using the spectral angle mapper (SAM) algorithm. In: Summaries of the Third Annual JPL Airborne Geoscience Workshop. Pasadena, California, USA, pp. 147–149.
Yu, L., Leng, G., 2022. Global effects of different types of land use and land cover changes on near-surface air temperature. Agric for Meteorol 327, 109232. https://doi.org/10.1016/j.agrformet.2022.109232.
Zhang, C., Ma, L., Chen, J., Rao, Y., Zhou, Y., Chen, X., 2019. Assessing the impact of endmember variability on linear Spectral Mixture Analysis (LSMA): A theoretical and simulation analysis. Remote Sens Environ 235, 111471. https://doi.org/10.1016/j.rse.2019.111471.